Synoptic Ozone, Cloud Reflectivity, and Erythemal Irradiance from Sunrise to Sunset for the Whole Earth as viewed by the DSCOVR spacecraft from Lagrange-1

Jay Herman[1], Liang Huang[2], Richard McPeters[3], Jerry Ziemke[3], Alexander Cede[4], Karin Blank[3]

Abstract

EPIC (Earth Polychromatic Imaging Camera) onboard the DSCOVR (Deep Space Climate Observatory) spacecraft is the first Earth science instrument located near the Earth-Sun gravitational plus centrifugal force balance point, Lagrange-1. EPIC measures Earth reflected radiances in 10 wavelength channels ranging from 317.5 nm to 779.5 nm. Of these channels, four are in the UV range 317.5, 325, 340, and 388 nm, which are used to retrieve O_3, 388 nm scene reflectivity (LER Lambert Equivalent Reflectivity), SO_2, and aerosol properties. Unlike low earth orbiting satellite instruments near noon values, these synoptic quantities for the entire sunlit globe from sunrise to sunset obtained every 68 minutes when it is summer or 110 minutes in winter at the receiving antenna in Wallops Island, Virginia. Depending on solar zenith angle, either 317.5 or 325 nm channels are combined with 340 and 388 nm to derive ozone amounts. As part of the ozone algorithm, the 388 nm channel is used to derive LER. The retrieved ozone amounts and LER are combined to derive the erythemal irradiance for the entire sunlit Earth's surface, 2048x2048 points, at a nadir resolution of 18 x 18 km^2 using a computationally efficient approximation to a radiative transfer calculation of irradiance. Corrections are made for altitude above sea level and for the reduced transmission by clouds based on retrieved LER.

[1]University of Maryland Baltimore County, Maryland

[2]Science Systems and Applications, Lanham, Maryland

[3]NASA Goddard Space Flight Center, Greenbelt, Maryland

[4]SciGlob Instruments and Services, Maryland

DSCOVR/EPIC Synoptic Ozone, Cloud Reflectivity, and Erythemal Irradiance From Sunrise to Sunset for the Whole Earth as viewed from an Earth-Sun Lagrange-1 Orbit

1.0 Introduction

The DSCOVR (Deep Space Climate Observatory) spacecraft was successfully launched on 11 February 2015 to a lissajous figure orbit near the Earth-Sun gravitational plus centrifugal force balance point, Lagrange-1 (L-1), $1.5x10^6$ km from the Earth. The earth pointing instruments on the DSCOVR spacecraft placed in orbit about the L-1 point will simultaneously observe the sun illuminated earth's disk from sunrise to sunset. An illustration of the orbit is given in the Appendix (see https://epic.gsfc.nasa.gov for details). DSCOVR started to transmit Earth data after it achieved a quasi-stable orbit in mid-June 2015. The DSCOVR mission at L-1 is at an optimum location for early warning solar flare observations (magnetic field, electron, and proton fluxes) from instruments contained on the sunward side of DSCOVR, and contains two Earth-viewing instruments allowing continuous observation of the sunlit face of the Earth. The EPIC (Earth Polychromatic Imaging Camera) instrument onboard DSCOVR images the Earth in ten narrow band wavelength channels (up to 2048 x 2048 pixels), producing both color images of the Earth and science data products such as ozone, SO_2, aerosol amounts, cloud reflectivity, UV surface irradiance, cloud and aerosol heights, and vegetation indices. This paper discusses the UV science products O_3, cloud reflectivity, and UV surface irradiance, methods of retrieval, and EPIC's UV in-flight calibration.

The data and images of the changing synoptic cloud cover from sunrise to sunset are unique to the EPIC satellite instrument. Neither geostationary nor low earth orbiting satellites can produce these data or images. Geostationary satellites could produce something similar, but to date, none have the UV channels for ozone and LER, and geostationary satellites are limited to a range of approximately $\pm 60^O$ latitude and $\pm 60^O$ longitude. While low earth orbiting satellite data can be combined to produce a global representation of ozone and cloud cover, all the ozone and cloud cover are for a fixed local time (e.g., 13:30 hours for OMI) and are not representative of the atmosphere at other times of the day.

1.1 EPIC Instrument

The EPIC instrument consists of a 30-cm aperture 283.642 cm focal length Cassegrain telescope containing a multi-element field-lens group focusing light onto a UV sensitive 2048 x 2048 hafnium coated CCD detector with 12 bit readout electronics. Images are made through ten narrow-band filters, four in the ultraviolet, four in the visible, and two in the near infrared. The 10 filter transmission functions are shown in Fig. 1. Observations are made as light passes sequentially through each of ten narrow-band filters mounted in two moveable filter wheels and through an exposure control 3-slot rotating shutter. The exposure times for each wavelength were adjusted in-flight to achieve an approximately 80 % CCD electron well fill in the brightest scenes, which were observed during the first week of operation, to avoid saturation and leaking from one pixel to another (blooming). Earth exposure times range from about 654 milliseconds at 317.5 nm to 22 milliseconds at 551 nm, which have not changed during the current life of the mission. Another set of exposure times was determined for viewing the full moon as seen from the Earth (Table 1). The CCD has a well depth of approximately $8.5x10^4$ electrons (a maximum signal to noise ratio SNR of 290:1) before a small dark current correction that is a function of its in-flight operating temperature of -20^{O}C. The 12-bit readout means that there are 2^{11} (2048) readout steps or counts (42 electrons/count). The counts divided by the exposure time (counts/second) are converted to radiances or albedos using in-flight scene matching calibration from low earth orbit satellites (see Sect. 1.2 and Table 2). The maximum SNR applies to the brightest of scenes over high clouds or fresh snow over ice. Cloud-free and snow-free scenes have much lower SNR, which affects the visible channels more than the UV channels because of the lower scene contrasts with clouds caused by enhanced UV Rayleigh scattering. There are occasional bright flashes caused by ice crystals in high clouds that saturate a few pixels (see Fig. 2 and Marshak et al., 2017) in the equatorial and mid-latitude regions.

The filters of interest for calculating ozone amounts, aerosol index, and cloud reflectivity are centered on 317.5, 325, 340, and 388 nm in the wavelength band with full widths at half maximum (FWHMs) 1.0, 1.0, 2.7, and 2.6 nm, respectively. For the UV channels, 2 x 2 individual pixels are averaged onboard the spacecraft to yield an effective 1024 x 1024 pixel image corresponding to an 18 x 18 km^2 resolution at the observed center of the Earth's sunlit disk. The effective spatial resolution decreases as the secant of the angle between EPIC's sub-earth point and the normal to the earth's surface. Only the 443 nm channel is retrieved at full resolution to help with resolving cloud cover and obtaining improved color images. The sampling resolution of a single pixel is about 8 x 8 km^2 (about 1 arcsecond), but including the effect of the optical point-spread function, the effective 443 nm channel resolution is about 10 km. The effective resolution at 443 nm has been verified by looking at clear scenes over the Nile River in Egypt and, occasionally, the cloud-free Amazon River in Brazil.

EPIC data has been obtained since June 15, 2015 at a rate of one set of 10 wavelengths every 68 minutes during Northern Hemisphere (NH) summer and one set every 110 minutes in the winter. The difference between summer and winter rates is caused by the reduced number of hours in the winter when the antenna (located at Wallops Island, Virginia) is in view of the spacecraft, and limitations from the spacecraft memory technology from the late 1990s.

Each of the 10 wavelength measurements is obtained at slightly different times. The first filter in the sequence is 443 nm, which takes about 2 minutes to complete a measurement (28 ms exposure time (Table 1) plus CCD readout and onboard processing time that includes 12-bit jpeg compression of a 2048 x 2048 pixel image). The remaining 9 filter measurements take a total of about 5 minutes (exposure times plus CCD readout into memory) and then another 13 minutes to process the data for the 9 filters (this includes 12-bit jpeg compression of 1024 x 1024 images that have been averaged onboard in groups of 2x2 pixels before compression). Adjacent pairs of wavelengths are measured at 30 second intervals before the onboard processing is started. This means the individual channel images are not co-located at the pixel level because of earth rotation (15.03^{O} per hour or about 1670 km per hour at the equator), the slow rotation of the spacecraft, 0.082^{O} per hour, and a small amount of spacecraft jitter). Each pixel views about 1 arc second or 2.78×10^{-4} degrees. Data from an onboard star-tracker and feedback from the earth's image on the CCD keep the images approximately centered on the CCD. The lack of native channel-to-channel colocation requires an elaborate spherical geometry geolocation analysis to adjust the data to a common latitude x longitude grid with an accuracy of 1/4 of a pixel.

A description of the EPIC instrument, its orbit, and some of the data products can be obtained from http://avdc.gsfc.nasa.gov/pub/DSCOVR/Web_EPIC/ and from http://epic.gsfc.nasa.gov/. The EPIC raw counts/second and science data (Version 2 used in this paper) are archived at https://eosweb.larc.nasa.gov/project/dscovr/dscovr_table in HDF5 format.

This paper presents examples of the ozone and scene reflectivity retrievals that are used to obtain unique estimates of erythemal UV irradiance (or UV Index, UVI) as a function of latitude, longitude, local solar time (LST), and altitude above sea level (ASL). Since this is the first paper on EPIC retrieved ozone, Sect. 1 contains a brief description of the calibration of the four UV channels and the ozone retrieval algorithm. Sect. 2 shows examples of natural color images, Sect. 3 gives an example of retrieved ozone and the corresponding 388 nm Lambert Equivalent Reflectivity (LER, Herman et al., 2009), Sect. 4 presents a validation of EPIC retrieved ozone compared to ozone from ground-based and satellite data, Sect. 5 shows details of the latitudinal and longitudinal synoptic variability of ozone, and Sect. 6 presents new results showing the sunrise to sunset variability of UV erythemal radiation reaching the Earth's surface including the reduction by clouds from sunrise to sunset.

1.2 Calibration

Before the raw EPIC data (counts per second) can be used, a number of pre-processing steps must be accomplished. The major steps are 1) measuring and subtracting the dark current signal, 2) "flat-fielding" the CCD so that the sensitivity differences between all four million pixels are determined and corrected, 3) correcting for stray-light effects to account for light that should be going to a particular pixel, but instead is scattered to different pixels, and 4) determining the radiometric calibration for each wavelength channel in terms of EPIC counts/second to be converted to earth normalized radiances or reflectances (backscattered at approximately 172^{O}). The earth upwelling normalized radiance I_M (W/(m^2 nm sr)) at the top of the atmosphere (TOA) is defined in terms of the albedo A_M given by Eq. 1,

$$A_M = \frac{I_M}{S_M/D_E^2} \quad (\mathrm{sr}^{-1}) \qquad (1)$$

for wavelength bands M=1 to 4, S_M is the incident solar irradiance (W/(m^2 nm)) weighted with the filter function for band M at 1 AU and D_E is the sun-earth distance in AU (astronomical units). Since EPIC does not measure solar irradiance, we use a high resolution solar irradiance spectrum, S(λ) (Dobber et al., 2008), as a reference solar spectrum. The reference spectrum is weighted with EPIC's filter transmission functions $T_M(\lambda)$ (Fig. 1) to obtain each EPIC channel's weighted solar irradiance S_M at solar-earth distance at 1 astronomical unit (Eqs. 1 and 2).

$$S_M = \int_{\lambda_1}^{\lambda_2} T_M(\lambda) S(\lambda) d\lambda \,/ \int_{\lambda_1}^{\lambda_2} T_M(\lambda) d\lambda \quad (\mathrm{Wm^{-2}nm^{-1}}) \qquad (2)$$

In-flight radiometric calibration is accomplished by comparison with albedo values measured by current well-calibrated LEO (low-earth orbiting; e.g., Aura/OMI, Ozone Monitoring Instrument, and Suomi-NPP/OMPS, National Polar-orbiting Partnership/Ozone Mapping and Profiler Suite) satellite instruments observing scenes that match in time and observing angles with those from EPIC. For albedo measurements, OMPS has a calibration accuracy of 2 %, while its wavelength dependence (precision) in the calibration is estimated to be better than 1 % (Jaross et al., 2014). The OMPS Nadir Mapper on Suomi-NPP has a 50 x 50 km^2 footprint in its normal operating mode with 36 cross-track views (±55^o satellite view angle or strip of about ±12^O equatorial longitude). It has a spectral resolution of 1 nm, which is close to EPIC's 317.5 nm and 325 nm channels FWHM, but narrower than EPIC's 340 nm and 388 nm channels. To perform in-flight calibration, OMPS' albedo spectra were either interpolated (for 317.5 and 325 nm channels) or convolved (at 340 and 388 nm) with each EPIC filter transmission function T_M (Fig. 1). Because the albedo spectra $A_M(\lambda)$ (Eq. 1) removes the Fraunhofer line structure contained in both the solar irradiance S_M and the reflected Earth radiance $I_M(\lambda)$, the interpolation and convolution of $A_M(\lambda)$ has better accuracy than directly using $I_M(\lambda)$. OMI on Aura has 13 x 24 km^2 spatial resolution and about ±56^o cross-track views (a strip of ± 1300 km or ± 13^O equatorial longitude) with a spectral resolution of 0.42 nm. To match measurements with DSCOVR, OMI's albedo spectra were convolved with EPIC's $T_M(\lambda)$. Then, the results in every two adjacent cross-track views and four consecutive along-track scans are combined to form 50 x 50 km^2 footprints for comparison with EPIC measured counts/second obtained from 7 x 7 EPIC pixels.

EPIC raw counts/second inside each coincident footprint are preprocessed by the steps stated in a previous paragraph. Then, the counts/second average and variance in each coincident footprint are computed to obtain the EPIC albedo calibration coefficients K_M (Eq. 3). Misalignment between EPIC and OMPS or OMI footprints can result in large scene noise unless uniform scenes are selected and less uniform scenes discarded. This is achieved by weighting each coincident data point with the reciprocal of the percent EPIC counts/second variance inside the coincident footprint. All of the coincident points between LEO satellites and EPIC observations occur within ±40^o of the earth's equator. Selected LEO footprints have viewing angles nearly identical to EPIC's (within 1^o in backscatter angle and 2^O degrees in solar zenith angle). EPIC's backscatter angle varies with latitude and longitude by less than 0.25^o, since the angular size of the earth varies from 0.45^O to 0.53^O to 0.45^O every 6 months depending on the location of DSCOVR in its orbit (an irregular Lissajous orbit about L-1 that is tilted relative to the ecliptic plane and perturbed by the Earth's moon). The orbit varies from 4^O to 15^O away from the Earth-Sun line. These small differences in observing geometry are corrected in the atmospheric radiative transfer model calculations $\alpha(\lambda)$ (Eq. 4), resulting in corrections less than 2 %. EPIC albedo calibration coefficients are derived from Eqs. 3 and 4.

$$K_M = \frac{A_M(OMPS)\{\alpha_M(EPIC)/\alpha_M(OMPS)\}}{C_M(EPIC)D_E^2} \tag{3}$$

$$\alpha_M = \int \alpha(\lambda) S(\lambda)\, T_M(\lambda)\, d\lambda \Big/ \int S(\lambda)\, T_M(\lambda)\, d\lambda \tag{4}$$

where

M is the EPIC channel number, M=1,2,3,4
A_M(OMPS) = OMPS albedo measurement in the EPIC channel-M wavelength band
α_M(EPIC) and α_M(OMPS) are computed albedo values for EPIC and OMPS coincident geometry,
C_M(EPIC) is the average count rate over the pixels matching OMPS,
D_E is the sun-earth distance in AU.
$\alpha(\lambda)$ is the computed high resolution normalized radiance spectrum,
$S(\lambda)$ is the referenced high resolution solar irradiance spectrum,
$T_M(\lambda)$ is the EPIC filter transmission profile or the OMPS slit function.

All of the coincidence points with LEO satellite instruments were measured using the area of the EPIC CCD within 600 pixels of its center. There are about 15000 coincidence data points accumulated by the end of 2016. Because of the large number of data points, statistical averaging errors are small. An atmospheric radiative transfer model, RTM, takes total column ozone and surface reflectivity from LEO retrievals to obtain both α_M(EPIC) and α_M(LEO). Although uncertainties in the RTM can propagate into the computed albedos, the resulting uncertainties in α_M(EPIC) and α_M(LEO) are approximately identical, and approximately cancel in Eq. 3. The resulting EPIC albedo calibration uncertainty is mostly inherited from the OMPS albedo calibration uncertainty, which has an accuracy of 2 % and a precision of 1 % in relative (wavelength dependent) values. For the UV channels, the calibration factors K_M are not constants, but are slowly increasing functions of time (on average 0.016 per year; see $K_M(t)$ in Fig. 2), which is normalized to one on 1 January 2016). Table 2 shows the reference values of K_M multiplied by π.

Using Tables 1, 2, and Fig. 2, EPIC albedo measurements are derived with

$$A_M(EPIC) = K_M C_M(EPIC) D_E^2 \tag{1-5}$$

Note that the factor D_E^2 for solar irradiance at 1 AU is contained in the albedo calibration coefficient K_M. Since solar activity changes (e.g., 27.5 day cycle) are negligible for EPIC UV channel wavelengths, daily solar irradiance changes are only adjusted with the sun-earth distance D_E. Users of EPIC data may also be interested in radiance measurements. The radiance calibration coefficients can be derived with Eq. 6,

$$E_M = K_M S_M \tag{6}$$

and the radiance measurements can be obtained with Eq. 7.

$$I_M(EPIC) = E_M C_M(EPIC) \tag{7}$$

The uncertainty in the radiance calibration can increase significantly due to errors in estimating the absolute solar irradiance. Uncertainty in estimated S_M for EPIC UV channels in Table 1 is about 3 %.

1.3 Ozone Algorithm

Once the albedo calibration factors are applied to EPIC's measured counts/second, the calculated albedos can be combined to retrieve total column ozone (TCO), Lambert Equivalent Reflectivity (LER), and aerosol index (AI). The TOA directional albedo calculation uses the TOMRAD radiative transfer calculation code, which has a spherical geometry correction for large solar zenith angles (SZA) and satellite looking angles (SLA) (Caudill et al., 1997). The calculation uses the same climatological ozone profiles used in OMI retrievals, altitude weighted average effective ozone temperatures, ground reflectivities, terrain height, and climatological cloud heights. Spectrally resolved O_3 absorption cross sections are from Brion et al., (1993, 1998); Daumont et al., (1992); and Malicet et al., (1995). The resulting spectra are convolved with the EPIC filter transmission functions (Fig. 1) and with the reference solar irradiance spectra (see Eq. 4).

The resulting computed α_M (Eq. 4) are compiled into a finely stepped look-up table as functions of ozone profiles and solar-view angles. EPIC ozone retrieval uses the 388 nm channel for computing the surface reflectivity with a formula similar (except for choice of wavelengths) to that used in cloud reflectivity studies (Herman et al., 2009). Then, the retrieval is based on two ozone absorption channels, 317.5 nm and 340 nm for low optical depth conditions, or 325 nm and 340 nm for high optical depth conditions, together with the 388 nm measurement to form triplet equations. The ozone retrieval algorithm assumes a linear wavelength dependence in the surface reflectivity (Eq. 8),

$$R_\lambda = R_{\lambda_0} + b(\lambda - \lambda_0) \qquad (8)$$

where λ_0 is given wavelength 388 nm. The total column ozone (TCO) is given by Eq. 9,

$$\Omega = \Omega_0 + \frac{\Delta N_{\lambda_1} \frac{\partial N_{\lambda_2}}{\partial R} (\lambda_2 - \lambda_0) - \Delta N_{\lambda_2} \frac{\partial N_{\lambda_1}}{\partial R} (\lambda_1 - \lambda_0)}{\frac{\partial N_{\lambda_1}}{\partial \Omega} \frac{\partial N_{\lambda_2}}{\partial R} (\lambda_2 - \lambda_0) - \frac{\partial N_{\lambda_2}}{\partial \Omega} \frac{\partial N_{\lambda_1}}{\partial R} (\lambda_1 - \lambda_0)} \qquad (9)$$

where

Ω_0 is an initial climatology estimate of TCO or TCO from previous step in the iteration,
λ_1 and λ_2 are the selected ozone absorption wavelengths,
N_λ is the N-value defined as logarithm of the albedo values by Eq. 10,

$$N_\lambda = -100\, log_{10}\{I_\lambda/(S_\lambda/D^2)\} \qquad (10)$$

and

ΔN_λ is the N-value residue (difference between the measured N-value and the computed N-value),

$\frac{\partial N_{\lambda_x}}{\partial Z}$ = measurement sensitivity with respect to the total column ozone, Z = Ω, or the surface reflectivity, Z = R, for wavelengths λ_1 or λ_2.

If one assumes the sensitivities to the surface reflectivity, $\partial N_\lambda/\partial R$ are wavelength independent, Eq. 5 for the triplet algorithm is similar to the Version 8 TOMS algorithm (Rodriguez et al., 2003).

Since the algorithm for ozone (Eqs. 8 to 10) requires the use of two or more wavelength channels, the measured counts/second for each channel must be geolocated on a common latitude x longitude grid that is accurate to 0.25 of a single pixel size. When projected on the 3-D Earth, the sampling size is about 8 km at nadir and effectively increases to 10 km when EPIC's point spread function is applied. The result for 2 x 2 pixel averaging is a spatial resolution at nadir of about 18 km, which gets larger as the secant of the SLA from the nadir point. SLA is measured relative to the normal to the Earth's surface, and is 0^O at nadir and almost 90^O at the Earth's sunlit terminator. The radiative transfer spherical geometry correction is accurate to about 80^O in SZA and SLA, which means that retrieved ozone values near the Earth's terminator are not accurate.

2 Natural Color Images

A typical eye response color image view of the Earth, obtained by a weighted combination of the geolocated red, green, and blue wavelength channels, is shown in Fig. 2. To produce RGB images adjusted to the human eye response, the algorithm used is a derivative of the International Commission on Illumination (CIE) process for estimating tristimulous values from calibrated instruments (Wyszecki and Stiles, 1982; Broadbent, 2004; Gardner, 2007; Bodrogi and Khanh, 2012). Obtaining eye response images for EPIC's narrow band filters (Table 1) was improved by customization of the algorithm to use additional channels than just the 443, 551, and 680 nm blue, green, and red channels.

Because the blue 443 nm channel is not spatially averaged onboard the spacecraft, the color images have a maximum resolution of about 10 km at nadir determined by looking at the discernable width of the Nile and Amazon Rivers. The color images also give an indication of the quality of the geolocation. Errors in geolocation would appear as pink edges at the cloud boundaries, which are not present in the images in Figs. 3 or in the complete image collection on http://epic.gsfc.nasa.gov/.

Even with accurate geolocation, about 0.25 pixels (2 km), between the 4 UV channels, there is some noise introduced into ozone retrievals by small cloud edge location errors when transferring all of the native data to a common latitude and longitude grid. Ozone retrievals over almost cloud-free scenes, such as over the Saharan desert or clear-sky portions of the oceans, show much less noise than those with partial cloud cover. Since the pixel-to-pixel noise caused by misaligned cloud edges is almost random, spatial averaging to about 50x50 km^2 (similar to TOMS and OMPS, but coarser than OMI spatial resolution) reduces the effect of apparent noise from cloud edges. The following sections use 25 x 25 km^2 spatial averaging (3 x 3 CCD pixels), which has more spatial details and some cloud-edge noise (noise < 3 %).

3 Examples of EPIC Ozone and Reflectivity

A matched pair of images for ozone and scene reflectivity LER (17 April 2016) are shown in Fig. 4 with a maximum resolution of 18 km, since all UV channels involved in the ozone retrieval are downlinked from the spacecraft at a resolution of 2 x 2 onboard averaged pixels. Note that the reduced resolution hdf5 data files stored on the ground are in their original sampling density (2048 x 2048), but have reduced spatial resolution. In Fig. 4, the entire data image for ozone and the LER scene reflectivity are all at a common Universal Time (00:36 UTC or 12:36 local time at the center of the image) and encompasses local times from sunrise (west) to sunset (east) with all images rotated so that north is up. In the LER scene, a large east-west belt of clouds are visible near the equator, as are cloud plumes descending from the Arctic. The major cloud patterns change slowly, but show major seasonal changes. Figure 5 shows six additional scenes from the same day, 17 April 2016, with large cloud features associated with the Arctic region, an equatorial cloud band, and large cloud structures over the Antarctic Ocean. Figure 6 shows reflectivity measurements for 23 November 2015 with cloud features common in the Southern Hemisphere SH. The cloud band extending toward the Antarctic region from Argentina's Salado River is an example of a persistent feature that appears frequently throughout the year. In a later section, the amounts of retrieved ozone and cloud reflectivity $0 < R_C < 1$ are used to estimate the amount of UV radiation reaching the earth's surface over snow/ice free scenes.

The Arctic and Antarctic ice sheets are visible after their spring equinox times, and especially in their respective late spring and summer images when the Earth's poles are tilted toward L-1 (Figs. 5 and 6). In the color and LER images, clouds over ice are not readily visible because of the very high ice reflectivity providing little or no contrast with 388 nm cloud reflectivity. It is possible to obtain information about clouds over ice from the O_2 A-band channel at 764 nm (Fig. 7), which differentiates between reflecting surfaces that are at different altitudes because of oxygen absorption in the atmosphere. In this image, the bright white clouds (less atmospheric O_2 absorption) are at higher altitudes than the grey clouds, which are all higher than the ice surfaces. A quantitative analysis of cloud height and cloud-caused reduction in solar irradiance reaching the ice surface will be the subject of a future paper.

4 Validation of EPIC Ozone Retrieval

EPIC retrieved ozone can be validated by comparison with other ozone measuring satellite data (e.g., OMI, and OMPS) and by comparison with well-calibrated ground-based instruments.

While EPIC observes from sunrise to sunset in every image, there are only 6 to 8 useful coincidences per 24 hours with a specified ground site separated by either 68 minutes (NH summer) or 110 minutes (NH winter). Coincidences at high SZA > 75^O are increasingly inaccurate for both satellite and ground-based retrievals. This problem is compounded for EPIC, since high SZA also implies high SLA, which increases the spherical geometry correction error. Ozone absorption and Rayleigh scattering at high SZA also prevents 317.5 nm radiances from reaching into the lower troposphere and to the surface, which is partially mitigated by having the retrieval algorithm automatically switch from 317.5 nm to 325 nm at high optical depths (usually high SZA).

A comparison of EPIC retrieved TCO with those determined by a Pandora spectrometer instrument (#034) located at Boulder, Colorado is shown in Fig. 8. This Pandora was selected because it has been extensively compared to a well calibrated Dobson spectroradiometer and to OMI and OMPS ozone overpass data (Herman et al., 2015). The Pandora data are matched in location and time t_O to the EPIC UTC when Boulder, Colorado is in view (several times per 24 hours). Pandora ozone is averaged over t_O ±12 minutes. EPIC data are limited to distances within 50 km of Boulder, Colorado. Figure 8 shows that EPIC and Pandora ozone amounts track each other closely during 2015 and 2016. The 2015-2016 average agreement is 2.7 ± 4.9 %. There is a period in the winter of 2016 where the Pandora data quality was degraded by the presence of heavy cloud cover and in February by a mechanical problem with the Pandora sun tracker.

The OMI and OMPS satellites are polar orbiting with an equator crossing time of about 13:30 hours local time measuring in a narrow strip on either side of the orbital track. While it is possible to compare EPIC ozone with low earth orbit satellite data, a more complete comparison can be made with the assimilated ozone product from MERRA-2, the Modern-Era Retrospective Analysis for Research and Applications, (Rotman et al., 2002) version 2 (MERRA-2, Molod et al., 2014). MERRA-2 ozone is based on Microwave Limb Sounder (MLS) and total column ozone from the Ozone Monitoring Instrument OMI on NASA's EOS *Aura* satellite. The advantage of using MERRA-2 is that the ozone field is synoptic and can be directly compared with EPIC for the same UTC (Fig. 9) over the same sunlit globe as seen by EPIC. The ozone structures seen by EPIC are all present in the MERRA-2 independent assimilation, even though there is an average offset of about 10 DU (3 %). The disagreement with EPIC is similar to the offset of MERRA-2 with other satellite data (Wargan et al., 2017). A close look at the ozone maps in Fig. 9 shows overall agreement with most features including the small region of elevated O_3 over the central US. There are differences, such as the higher amount of O_3 measured by EPIC over Brazil on 23 November and the structure at 15^ON in the transition from equatorial O_3 values to mid-latitude values (dark blue to light blue).

5.0 Synoptic Variation of Ozone (SVO) from Sunrise to Sunset

Most LEO satellite views of ozone are at almost fixed local time based on the equator crossing local solar time (13.5 ± 0.8 hours side scanning) with approximately 20 minutes local time variation from the equator to the pole. Longitudinal coverage is obtained by piecing together North-South strips obtained about 90 minutes apart. Variation that occurs on a scale less than 90 minutes cannot be seen from a polar orbiting LEO satellite, nor can variation from different local times of the day. EPIC observes from close to sunrise and sunset with local solar noon near the center of the data set as shown in Fig. 10. The exact position of noon in the EPIC images depends on the location of EPIC in its orbit relative to the Earth-Sun line. The longitude resolution is approximately 0.25^O at the center of the FOV, which corresponds to a time resolution of about 1 minute. The resolution decreases as the secant of the angle from the center (e.g., 2 minutes or 0.5^O at 60^O from the center). A limitation in the EPIC observations occurs at high SZA and high SLA. As can be seen in Fig. 10, ozone values near the morning terminator are probably too low compared to the middle longitude values. These retrieval errors are partly caused by the effects of spherical geometry that are not properly represented in the TOMRAD radiative transfer calculations.

The view of the EPIC instrument from sunrise to sunset at fixed UTC is not the diurnal variation that an instrument on the ground would see from sunrise to sunset. For the ground-based Pandora instrument, the observed changes throughout the day from sunrise to sunset are at varying UTC every 80 seconds. Compared to the ground-based viewpoint, EPIC obtains data for a fixed geographic location every 68 minutes UTC in NH daytime summer and every 110 minutes in NH daytime winter.

5.1 Southern Hemisphere SH Late Spring 23 November 2015 :

To illustrate the SH synoptic change in ozone, Figs. 10 and 11 show the diurnal (longitudinal) variation of ozone centered on the South American continent on 23 November 2015 at 16:20 UTC. The local time varies from early morning (06:20, -150^{O} longitude) to late-afternoon (16:20, 0^{O} longitude). At high southern latitudes, 60^{O}S and 70^{O}S, the late spring (23 November) residue of 2015 Antarctic ozone hole is clearly visible in the ozone map image (Fig. 10). Figure 11 shows details of the ozone amounts in specified latitude bands (±0.125^{O} wide) in the Southern Hemisphere sampled every 5^{O} degrees from 0^{O} to 70^{O}S. Solar zenith angles are limited to the range ±70^{O} to avoid high latitudes and longitudes near sunrise or sunset where spherical geometry effects become important. This particular example (Fig. 11) is from one image centered over South America (Fig. 10). For 23 November there are 15 more overlapping images covering the entire 360^{O} of longitude that could be combined to produce a complete composite global map of ozone at 15 different UTCs. In the NH summer there would be 22 images per day. A composite ozone map of this kind would no longer be synoptic, since overlapping data are averaged, but would now be similar to the joined data strips from OMI or OMPS.

Figure 11 contains the data points from a 0.25^{O} x 0.25^{O} average within each 5^{O} latitude band L shown as light grey dots. The dark lines are a Lowess(0.05) fit (locally weighted least squares fit to 5 % of the data, (Cleveland, 1981)), which corresponds to approximately a 30 minute time average (7.5^{O} Longitude). The largest apparent scatter from the Lowess fit occurs at L = 0.125^{O}S, which amounts to a longitudinal standard deviation from the mean of ±4 DU or ±1.5 %.The equatorial bands (0^{O}S to 20^{O}S) shows considerable longitudinal change (10–20 % from L = 0–40^{O}S rising to 75 % at L = 70^{O}S, approximately as $TCO = 16.063 + 0.56L + 0.02L^2$). Most of the observed changes are dynamically driven, since the photochemistry involved in the stratosphere (20 - 25 km altitude) is too slow to produce such large changes with changing SZA. Southward of 45^{O}S, the effects of the remaining ozone hole depletion (dark blue in Fig. 10), which is still present in November, appear at -50^{O} longitude as indicated in Fig. 11.

5.2 Northern Hemisphere NH Summer Solstice 21 June 2016:

An example is provided for the ozone retrievals obtained on 21 June 2016 at 18:41 UTC that is approximately centered over North America (Fig. 12). Since this is Northern Hemisphere summer solstice, corresponding to the sun being nearly overhead at 23^{O}N, the latitude range available for retrieving ozone extends over the North Pole. Figure 13 contains ozone retrievals in 0.25^{O} wide latitude bands similar to Fig. 11. Unlike the SH 23 November 2015 example, there is only moderate longitudinal (diurnal) variability in ozone amount for latitudes between 0^{O} and 15^{O}N. However, there is a clear wave structure in the 20^{O}N to 25^{O}N bands with a periodicity of approximately 35^{O} longitude (2.3 hours) and again in the 40^{O}N to 60^{O}N bands that are not obvious in the global map (Fig. 12).

The dynamical effects on ozone in the NH mid-latitudes are quite different than their counterparts in the SH, where the NH mid-latitude behavior (30^{O}N–35^{O}N) is clearly separated from equatorial and high latitude bands with an increase in ozone amount from about 280 DU to about 350 DU, which is larger than a similar increase in the SH. There is an ozone periodicity of approximately 38^{O} longitude (2.5 hours) at 30^{O}N–35^{O}N midday and a longer longitudinal period 73^{O} (4.9 hours) in the morning. At higher latitudes, 35^{O}N–55^{O}N, the variability is more pronounced with an approximate period of 55^{O} (3.6 hours). In the bands from 55^{O}N–70^{O}N the variability is reduced and the ozone amount falls from mid-latitude values of about 350 DU to below 300 DU. The wave structure varies throughout the year in both hemispheres.

5.3 Northern and Southern Hemisphere 17 April 2016 18:35 UTC

Figure 5-5 shows the ozone retrieval for the sunlit globe on 17 April 2016 at 18:36 UTC about 1 month from the March equinox including large plumes of elevated ozone amounts (450 DU) extending from high latitudes into mid-latitudes where the usual ozone amount is about 350 DU. For the SH (Fig. 5-5), polar ozone variability (280-320 DU) is relatively small compared to November 23 (Fig. 10). There is wave structure (Fig. 15) between 30^{O}S and 40^{O}S with a periodicity of about 4 hours (60^{O} longitude) (see also Schoeberl and Kreuger, 1983). The dip in O_3 amount at 77^{O}W to 67^{O}W and 10^{O}S to 25^{O}S corresponds to the Andes Mountains in Peru, Bolivia, and Chile. While the SZA range is limited to ±70^{O}, the SLA reaches more than 80^{O} at low latitudes for longitudes between 40^{O}S and 20^{O}S introducing spherical geometry correction errors that increase towards sunset near 20^{O}W. The errors appear as apparent increases in O_3 amount. At higher latitudes, the SLA is in the middle 70^{O}s when the SZA is 70^{O}. The high SLA error is present in both hemispheres for observations near equinox.

The NH shows little variability in the equatorial region (0–25^{O}N) with a mean value of about 260 DU (Fig. 16). The SLA error is present for latitudes between 0 and 15^{O}N and 0 and 15^{O}S that appears as an elevated ozone amount at longitudes east of 50^{O}W. Mid-latitudes (30^{O}N to 40^{O}N) show a wave structure that is approximately 37^{O} apart (2.5 hours) at 35^{O}N. A similar structure occurs in the SH with a period of about 4.5 hours. There is an ozone maximum (red area in Fig. 14 about 450 DU) near 140^{O}W extending from 60^{O}N to 35^{O}N, very high ozone amounts in the Arctic region, and a high ozone patch over the central US (35^{O}N to 45^{O}N and 104^{O}W) peaking at 420 DU (40^{O}N and 104^{O}W), which probably corresponds to a region of high atmospheric pressure.

6.0 Estimating erythemal Irradiance at the Earth’s Surface

The unique observing geometry of DSCOVR/EPIC permit the use of synoptic ozone and cloud reflectivity data to be used to compute the diurnal variation of UV irradiance from sunrise to sunset for any point on the illuminated earth observed by EPIC. Previous calculations from satellite data used cloud cover and ozone from 13:30 and assumed it applied to local noon. The assumption is usually adequate for slowly varying ozone, but not for estimating the effects of more rapidly varying cloud cover. The following paragraphs discuss the calculation of erythemal irradiance, a spectrally weighted mixture of UV wavelengths used as a measure of skin reddening and potential sunburn from exposure to sunlight.

Erythemal irradiance E_0(SZA θ, C_T) at the earth sea level (watts/m^2) is defined in terms of a wavelength dependent weighted integral over a specified weighting function $A(\lambda)$ times the incident solar irradiance $I(\lambda,\theta,\Omega,C_T)$ (Watts/m^2) (Eq. 11) at the Earth's sea level. The erythemal weighting function $Log_{10}(A_{ERY}(\lambda))$ is given by the standard erythemal fitting function shown in Eq. 12 (McKinley and Diffey, 1987). Tables of radiative transfer solutions for D_E = 1 AU are generated for a range of sza ($0 < \theta < 90^O$), for ozone amounts $100 < \Omega < 600$ DU, and terrain heights $0 < Z < 5$ km using the TUV DISORT radiative transfer model as described in Herman (2010) for erythemal and other action spectra (e.g., plant growth, vitamin D production, cataracts, etc.).

$$E_0(\theta,\Omega,C_T) = \int_{250}^{400} I(\lambda,\theta,\Omega,C_T)A(\lambda)d\lambda \qquad (11)$$

$$\begin{array}{ll} 250 < \lambda < 298 \text{ nm} & Log_{10}(A_{ERY}) = 0 \\ 298 < \lambda < 328 \text{ nm} & Log_{10}(A_{ERY}) = 0.094\,(298 - \lambda) \\ 328 < \lambda < 400 \text{ nm} & Log_{10}(A_{ERY}) = 0.015\,(139 - \lambda) \end{array} \qquad (12)$$

Equation 11 can be accurately approximated by the power law form (Eq. 13), where $U(\theta)$ and $R(\theta)$ are fitting coefficients to the radiative transfer solutions in the form of rational fractions. Rational fractions were chosen because they tend to behave better at the ends of the fitting range than comparable fitting accuracy polynomials.

$$E_0(\theta,\Omega,C_T) = U(\theta)\,(\Omega/200)^{-R(\theta)}C_T \qquad (13)$$

$$U(\theta) \text{ or } R(\theta) = (a+c\theta^2+e x^4)/(1+b\theta^2+d\theta^4+f\theta^6) \quad r^2 > 0.9999 \qquad (14)$$

$$C_T = (1-LER)/(1-R_G) \text{ where } R_G \text{ is the reflectivity of the surface} \qquad (15)$$

$$E(\theta,\Omega,Z) = E_0(\theta,\Omega)\;H(\theta,\Omega,z) \qquad (16)$$

$$H(\theta,\Omega,Z) = 1+(0.04652\,Z_{km} +0.00496)\,(-0.07033\,(\Omega/200) + 1.12303)G(\theta) \qquad (17)$$

$$G(\theta) = g+h\theta+i\theta^2+j\theta^3+k\theta^4 \qquad (18)$$

The coefficients a, b, c, d, e, f, g, h, j, and k are in Tables A-1 and A-2 in the appendix

The E_0 solutions to the radiative transfer calculations can be accurately reproduced by a relatively simple functional form (Eqs. 13 to 15) with the coefficients given in Table A-1. These are the same coefficients given in Herman (2010) along with other biological action spectra weighting functions, $H(z,\theta)$ is a function representing the increase in $E(\theta,\Omega,Z)$ with altitude per km, and C_T is the cloud transmission function (Eq. 15) estimated from the retrieved LER derived by assuming that the cloud-ground system can be approximated by a two-layer Stokes problem (elevated cloud and surface) with atmospheric effects between the cloud bottom and the surface neglected (Herman et al.,2009). r^2 is a measure of the correlation of the E_0 data points with the fitting function. Eqs. 13 to 18 are for an Earth-Sun distance of 1 AU.

For E_0 The fitting residual is less than ± 0.001 W/m^2 compared to the worst case when E_0(50^o, 200) = 0.15 W/m^2 (Herman, 2010). When height effects are included $E(\theta,\Omega,Z) = E_0(\theta,\Omega)\ H(\theta,\Omega,Z)$, where $H(\theta,\Omega,Z)$ is a fitting polynomial (Eq. 17) to the downward irradiance at 0, 1, 2, 3, 4, and 5 km based on results from the radiative transfer calculation. The increase of erythemal irradiance with altitude has an SZA dependence given by $G(\theta)$, which increases with θ until θ is approximately 60^O, and then $G(\theta)$decreases.

The height dependence of $E(\theta,\Omega,Z)$ is similar to that derived by Chubarova et al. (2016) for low aerosol amounts. When absorbing aerosols have a significant optical depth, Chubarova et al. (2016) derived a multiplicative correction term to $E(\theta,\Omega,Z)$ for a wide variety of conditions.

When Eq. 13 is applied to the ozone and LER data described in previous sections, the global erythemal irradiance at the ground can be obtained after correction for the Earth-Sun distance D_E in a manner similar to Eq. 1, where D_E in AU can be approximated by (Eq. 19),

$$D_E = 1 - 0.01672 \cos(360\ (\text{day\_of\_year} - 4)/365.25) \quad (19)$$

An example of $E(\theta,\Omega,Z)$ is shown in Fig. 17 for 17 April 17 2016 at 18:35 UTC. Local noon is near the center of the image with sunrise to the left (west) and sunset to the right (east). For this date, the sun is overhead just north of the equator producing very high values of erythemal irradiance $E(\theta,\Omega,Z)$ corresponding to a UV index, UVI, of 13 at sea level in the Pacific Ocean (UVI = 40 $E(\theta,\Omega,Z)$). The UVI scale was designed for sea level mid latitudes ranging from 0 to 10 to provide public health warnings (e.g. for UVI = 8). Somewhat higher values are seen in the Sierra Nevada Mountains in Mexico near 20^{O}N. This particular day is relatively cloud free over most of South America except for clouds over southern Brazil extending into Paraguay and other small patches of clouds. For the erythemal irradiance, the presence of clouds reduces the amount of UV reaching the ground (blue color with a UV index of less than 4).

The increase with altitude is much more pronounced during the summer months over the Andes Mountains reaching above 4 km (over 13,000 feet). Figures 18 and 19 show the large increases with altitude over the Andes Mountains for 23 November 2015, with the sun nearly overhead at 20^{O}S latitude. Here the UV index ranges from 16 to 18, which agrees with previous ground-based measurements in this region (Cede et al., 2002). Any significant unprotected exposure to these levels of UV would lead to severe sunburn and eye damage. On a completely clear day the UV index would be even higher than 18. Figure 19 is a longitudinal slice through the UV data in Fig. 18 at 20^{O}S. The figure shows the longitudinal variation $E(\theta,\Omega,Z)$ as a function of local time, the effect of light clouds on the eastern side of the Andes Mountains, and the sharp reduction at 50^{O}W.

Figure 20 shows the erythemal irradiance computed for 21 June 2016 centered over the US and Central America. The sun is overhead at 23.3^{O}N latitude. In the clear regions not covered with light clouds, the UV index reaches about 12 extending from an area in the Pacific Ocean at 15^{O}N up into the US mid-west, Rocky Mountains, Utah and New Mexico. The eastern US has a lower UV index of about 8.

The extended scale of this map (UVI = 0 to 20) is too coarse to see the variation with latitude on the east coast.

Similarly, Fig. 21 shows high values of erythemal irradiance in the Himalayan Mountains on June 21, 2016 with peak UV index of about 15 even in the presence of partial cloud cover that reflects a portion of the incident solar flux back to space. The effect of cloud cover can be seen in Fig. 22, which is a longitudinal slice through the irradiance values associated with the latitude at 32^{O}N. In the absence of clouds, the peak value of the UV index would be close to 20. Even with cloud cover, the UV index reached 15, which is twice the value of a typical cloudless summer case in the US at comparable latitude.

7.0 Summary

The DSCOVR/EPIC 10-filter Spectroradiometer (317.5 to 780 nm) makes measurements of the the rotating sunlit face of the earth from the Lagrange-1 point located $1.5x10^{6}$ km from the earth with a maximum resolution of 10 x 10 km^2 for 443 nm at the sub-satellite point. The other 9 channels have 18 x 18 km^2 resolution. The key difference between EPIC and LEO satellites is EPIC's ability to measure the whole sunlit earth (sunrise to sunset) at the same UTC (synoptic measurements) every 68 or 110 minutes depending on the season at the Wallops Island, Virginia data receiving station. EPIC ozone retrievals have been compared successfully to both ground-based Pandora spectrometer instruments and to the MERRA-2 satellite data assimilation model for the same UTC observed by EPIC. EPIC's synoptic measurements ensure that the ozone amounts, cloud reflectivity, and aerosol amounts that are used to estimate UV irradiance are the proper values for each time of the day. EPIC has been making measurements since June 15, 2015 with no evidence of significant degradation relative to LEO satellites observing the same scene at the same angles. EPIC has obtained ozone and reflectivity data multiple times per 24 hours for over two years that can be used to more accurately estimate the health effects from continuous or periodic exposure during any day to UV radiation reaching the ground including the effects of cloud cover and altitude.

Appendix

Figure A1 illustrates the orbit of the DSCOVR spacecraft following the earth in its orbit about the sun.

Table A-1 Coefficients R(θ) and scaling coefficient U(θ) for $0 < \theta < 80^{O}$ and $100 < \Omega < 600$ DU for $E(\Omega,\theta) = U(\theta)\,(\Omega/200)^{-R(\theta)}$ (1.0E10 = $1.0\text{x}10^{10}$)

$$U(\theta) \text{ or } R(\theta) = (a+c\theta^2+e\theta^4)/(1+b\theta^2+d\theta^4+f\theta^6) \quad r^2 > 0.9999$$

Action Spectra	$U(\theta)$ (watts/m^2)	$R(\theta)$
CIE Erythemal U_{ERY} & R_{ERY}	a= 0.4703918683355716 b= 0.0001485533527344676 c= -0.0001188976502179551 d= 1.915618238117361E-08 e= 7.693069873238405E-09 f= 1.633190561844982E-12	a= 1.203020609002682 b= -0.0001035585455444773 c= -0.00013250509260352 d= 4.953161533805639E-09 e= 1.897253186594168E-09 f= 0.0

Table A-2 Solar Zenith angle function G(θ) used in Eq. 18

$$G(\theta) = g+h\theta+i\theta^2+j\theta^3+k\theta^4$$

g= 0.9996074048174048	j= 1.412462444962443E-06
h= 0.0001453776871276851	k= -2.037907925407924E-08
i= 2.806514180264192E-05	

References

Bodrogi, Peter and Tran Quoc Khanh, Illumination, Color and Imaging: Evaluation and Optimization of Visual Displays, Wiley-VCH Verlag GmbH & Co. KGaA. 2012.

Brion, J., Chakir, A., Daumont, D., Malicet, J., and Parisse, C.: High-resolution laboratory absorption cross section of O3. Temperature effect, Chem. Phys. Lett., 213, 610–612, 1993.

Brion, J., Chakir, A., Charbonnier, J., Daumont, D., Parisse, C., and Malicet, J.: Absorption spectra measurements for the ozone molecule in the 350–830 nm region, J. Atmos. Chem., 30, 291–299, 1998.

Broadbent, Arthur D. A critical review of the development of the CIE1931 RGB color-matching functions, Color Research & Applications. 29 (4): 267–272. doi:10.1002/col.20020, 2004

Cariolle, D., and M. Déqué (1986), Southern hemisphere medium-scale waves and total ozone disturbances in a spectral general circulation model, J. Geophys. Res., 91(D10), 10825–10846, doi:10.1029/JD091iD10p10825 1986.

Caudill, T.R., D.E. Flittner, B.M. Herman, O. Torres, and R.D. McPeters, Evaluation of the pseudo-spherical approximation for backscattered ultraviolet radiances and ozone retrieval, J. Geophys. Res., 102, 3881-3890, 1997.

Cede, A., E. Luccini, R.D. Piacentini, L. Nuñez, and M. Blumthaler, Monitoring of Erythemal Irradiance in the Argentine Ultraviolet Network, J. Geophys. Res., 107 (D13), 10.1029/2001JD001206, 2002.

Cleveland, William S., LOWESS: A program for smoothing scatterplots by robust locally weighted regression. The American Statistician. ***35*** *(1): 54.* JSTOR 2683591. doi:10.2307/2683591, 1981.

Daumont, D., Brion, J., Charbonnier, J., and Malicet, J.: Ozone UV spectroscopy I: Absorption cross-sections at room temperature,J. Atmos. Chem., 15,145–155, 1992.

Dobber, M., Voors, R., Dirksen, R., Kleipool, Q., and Levelt, P., 2008, The high resolution solar reference spectrum between 250 and 550 nm and its application to measurements with the Ozone Monitoring Instrument. Solar Phys., 249, 281–291, 2008.

Gardner, James L., Comparison of Calibration Methods for Tristimulus Colorimeters, Journal of Research of the National Institutes of Standards and Technology. **112** (3): 129–138. doi:10.6028/jres.112.010, 2007.

Herman, J.R., G. Labow, N.C. Hsu, D. Larko (2009), Changes in Cloud Cover (1998-2006) Derived From Reflectivity Time Series Using SeaWiFS, N7-TOMS, EP-TOMS, SBUV-2, and OMI Radiance Data, J. Geophys. Res., 114, D01201, doi:10.1029/2007JD0008, 2009.

Jaross, G., P. K. Bhartia, G. Chen, M. Kowitt, M. Haken, Z. Chen, P. Xu, J. Warner, and T. Kelly (2014), OMPS Limb Profiler instrument performance assessment, J. Geophys. Res. Atmos., 119, 4399–4412, doi:10.1002/2013JD020482, 2014.

Madronich, S., McKenzie, R.L., Björn, L.O. and Caldwell, M.M. (1998), "Changes in biologically active ultraviolet radiation reaching the Earth's surface," *Photochem. Photobiol.* **46**, 5-19, 1998.

Malicet, J., Daumont, D., Charbonnier, J., Chakir, C., Parisse, A.,and Brion, J.: Ozone UV Spectroscopy.II: Absorption cross sectionsand temperature dependence, J. Atmos. Chem., 21, 263–273, 1995.

Marshak, A., T., Várnai, and A., Kostinski (2017), Terrestrial glint seen from deep space: Oriented ice crystals detected from the Lagrangian point, Geophys. Res. Lett., 44, doi:10.1002/2017GL073248, 2017.

McKinley, A. F., and B. L. Diffey (1987), A reference action spectrum for ultraviolet induced erythema in human skin, in Human Exposure to Ultraviolet Radiation: Risks and Regulations, edited by W. R. Passchier and B. F. M. Bosnjakovic, pp. 83 – 87, Elsevier, Amsterdam, 1987.

Molod, A., Takacs, L., Suarez, M., and Bacmeister, J., 2014: Development of the GEOS-5 atmospheric general circulation model: evolution from MERRA to MERRA-2, Geosci. Model Dev. Discuss., 7, 7575-7617, doi:10.5194/gmdd-7-7575-2014.

Rodriguez, Juan V., ; Colin J. Seftor ; Charles G. Wellemeyer and Kelly Chance (2003), "An overview of the nadir sensor and algorithms for the NPOESS ozone mapping and profiler suite (OMPS)", Proc. SPIE 4891, Optical Remote Sensing of the Atmosphere and Clouds III, 65 (April 9, 2003); doi:10.1117/12.467525; http://dx.doi.org/10.1117/12.467525, 2003.

Rotman, D.A., J.R. Tannahill, D.E. Kinnison, P.S. Connell, D. Bergmann, D. Proctor, J.M. Rodriguez, S.J. Lin, R.B. Rood, M.J. Prather, P.J. Rasch, D.B. Considine, R. Ramaroson, S.R. Kawa (2001), The Global Modeling Initiative assessment model: Model description, integration and testing of the transport shell, J. Geophys. Res., 106, 1669-1691, 2001.

Schoeberl, M.A. and A. J. Krueger, Medium Scale Disturbances in Total Ozone During Southern Hemisphere Summer," *Bull. Amer. Met. Soc.,* 1358, 1983.

Tzortziou, M., **J. R.** Herman, A. Cede, and N. Abuhassan (2012), High precision, absolute total column ozone measurements from the Pandora spectrometer system: Comparisons with data from a Brewer double monochromator and Aura OMI, J. Geophys. Res., 117, D16303, doi:10.1029/2012JD017814, 2012.

Wargan, Krzysztof, Gordon Labow and Stacey Frith, Steven Pawson, Nathaniel Livesey, Gary Partyka, Journal of Climate 30, DOI: http://dx.doi.org/10.1175/JCLI-D-16-0699.1, 2017.

Wyszecki, Gunther and W. S. Stiles, Color Science: Concepts and Methods, Quantitative Data and Formulae, 2nd Edition, ISBN: 978-0-471-39918-6, John Wiley and Sons, 1982.

Tables

Table 1 Exposure Times for viewing the Earth and Full Moon (Earth side view)

Wavelength	Earth Exposure (ms)	Full Moon Exposure(ms)	Filter Width (nm FWHM)
317.5	654	2500	1
325	442	500	1
340	67	92	2.7
388	87	95	2.6
443	28	100	2.6
551	22	70	3
680	33	105	1.6
688	75	224	0.84
764	101	250	1.0
779.5	49	180	1.8

Table 2 πK_M on 1 January 2016 Irradiance at 1 AU

M	λ (nm)	πK_{MO}	S_M(mW/m^2/nm)
1	317.478	1.216E-04	819.0
2	325.035	1.111E-04	807.7
3	339.858	1.975E-05	995.8
4	387.923	2.685E-05	1003.

Table A1 Coefficients R(θ) and scaling coefficient U(θ) for $0 < \theta < 80^{O}$
and $100 < \Omega < 600$ DU for $E(\Omega,\theta) = U(\theta)\,(\Omega/200)^{-R(\theta)}$ (1.0E10 = 1.0×10^{10})

$$U(\theta) \text{ or } R(\theta) = (a+c\theta^2+e\theta^4)/(1+b\theta^2+d\theta^4+f\theta^6) \quad r^2 > 0.9999$$

Action Spectra	$U(\theta)$ (watts/m^2)	$R(\theta)$
CIE Erythemal U_{ERY} & R_{ERY}	a= 0.4703918683355716 b= 0.0001485533527344676 c= -0.0001188976502179551 d= 1.915618238117361E-08 e= 7.693069873238405E-09 f= 1.633190561844982E-12	a= 1.203020609002682 b= -0.0001035585455444773 c= -0.00013250509260352 d= 4.953161533805639E-09 e= 1.897253186594168E-09 f= 0.0

Table A2 Solar Zenith angle function $G(\theta)$ used in Eq. 18

$$G(\theta) = g+h\theta+i\theta^2+j\theta^3+k\theta^4$$

g= 0.9996074048174048

h= 0.0001453776871276851

i= 2.806514180264192E-05

j= 1.412462444962443E-06

k= -2.037907925407924E-08

Figure Captions

f01 Filter transmission functions (percent) for the 10 EPIC wavelengths based on laboratory measurements done in air. The central wavelength label is the shifted value used for the instrument in the vacuum of space.

f02 Normalized calibration functions referenced to their value at 4 Jan 2016 when D_E = 1 au. Average rate of increase is 0.016 per year.

f03 Natural Color EPIC Earth images from June 6 and December 6, 2016 showing the field of view during the respective hemispheric summers. In both of these images, 6 months apart, the EPIC orbit is to the west of the Earth-Sun line causing the west side of the globe (sunrise) to appear brighter than the east side (sunset). Notice the bright specular reflection over Argentina, South America embedded within a cloud feature. This is thought to be from ice crystals in high clouds (Marshak et al., 2017).

f04 EPIC retrieved ozone and LER values for April 17, 2016 at 00:36 UTC. The ozone scale is from 100 to 500 DU, and the LER scale is from 0 to 100 percent.

f05 LER at six sequential UTC 0:36, 2:24, 4:12, 6:00, 7:48, and 9:36 from 17 April 2017 showing clouds in the arctic region as the earth rotates in EPIC's field of view.

f06 Cloud formations from 23 Nov 2015 showing cloud cover in the Southern Hemisphere and near Antarctica at 6 different UTC's, 10:56, 12:44 14:32, and 16:20, 14:32, 18:09, and 19:57.

f07 O_2 A-band View of Antarctica on December 6, 2015 showing clouds over ice. The white bright clouds are at higher altitudes than the dull grey clouds because of a combination of less oxygen absorption and higher optical depth.

f08 Daily O_3 data for EPIC (red) and Pandora (Grey) 2015 - 2016. Left: EPIC ozone data compared to Pandora retrievals at Boulder Colorado. Right: Percent difference between EPIC and Pandora.

f09 Comparison of EPIC total column ozone with the MERRA-2 assimilation model ozone.

f10 Global image of ozone field for Fig. 11 for 23 Nov 2015 at 16:20 UTC

f11 Longitudinal or diurnal variation of ozone for the Southern Hemisphere every 5^O degrees from 0^O to $70S^O$ for 23 Nov 2015 at 16:20 UTC. The grey points are the individual data points in the band. The solid lines are a Lowess(0.05) fit to the data points representing a solar time average from 0.6 to 0.7 hours depending on latitude. The SZA is limited to $\pm 70^O$. Longitude = 0 Corresponds to 16:20 local time and longitude = -150 corresponds to 06:20 local time.

f12 Global image of ozone field for Fig. 13 for 21 June 2016 at 18:41 UTC

f13 Longitudinal or diurnal variation of ozone for the Northern Hemisphere every 5^O from 0^O to 70^O for 21 June 2016 at 18:41 UTC. The grey bands are the individual data points in the band. The solid lines are a Lowess(0.05) fit to the data points representing a solar time average from 0.6 to 0.7 hours depending on latitude. The SZA is limited to ±70^{O}. Longitude = 0 Corresponds to 18:41 local time and longitude = -180 corresponds to 06:41 local time.

f14 Global image of ozone field for Figs. 15 and 16 for 17 April 2016 at 18:36 UTC.

f15 Southern Hemisphere: Solid lines are approximately 30 minute averages in solar time at 18:38 UTC on 17 April 2016 for ozone variation between 0^{O} and 55^{O}S latitude in 0.25^{O} latitude bands for 17 April 2016 at 17:36 UTC.

f16 Northern Hemisphere: Solid lines are approximately 30 minute averages in solar time at 18:38 UTC on 17 April 2016 for ozone variation between 0^{O} and 75^{O}N latitude in 0.25^{O} latitude bands for 17 April 2016 at 17:36 UTC.

f17 Erythemal irradiances calculated from Eq. 13 and from the EPIC ozone and LER data obtained on April 17, 2016 at 18:35 UTC. The scale shows both the irradiance values in W/m2 and the UV index ranging from 0 to 20. This scene is centered over the Pacific Ocean and shows a peak UV index of about 15. Since this period is close to equinox, the sun is nearly overhead just north of the equator with solar noon at 98.75^{O}W longitude and overhead near 10^{O}N.

f18 Erythemal irradiances centered over South America on November 23, 2015 at 16:19 UTC showing extremely high values in the Andes Mountains in Peru, Bolivia, and Chile corresponding to a UV index greater than 20. Local solar noon is at 64.75^{O}W and overhead near 20^{O}S.

f19 Erythemal Irradiances in a longitudinal slice at 20^{O}S through a peak occurring in the Andes mountains. Local noon is at 64.75^{O}W.

f20 Erythemal irradiances centered over the United States on June 21, 2016 showing high values over the Rocky Mountains and a portions of the Sierra Nevada Mountains. The UV index reaches about 15. Local solar noon is at 99.75^{O}W and overhead near 23.3^{O}N.

f21 Erythemal UV irradiances centered over the Indian Ocean on June 21, 2016 showing high values over the Himalayan Mountains with the UV index exceeding 14. UV levels are moderated by partial cloud cover reflection of radiation back to space. Solar noon is at 80.25^{O}E.

f22 Erythemal Irradiances in a longitudinal slice at 32^{O}N through a portion of the Himalayan mountains. Local solar noon is at 80.25^{O}E.

fA1 An illustration of DSCOVR’s Lagrange-1 orbit

Figures

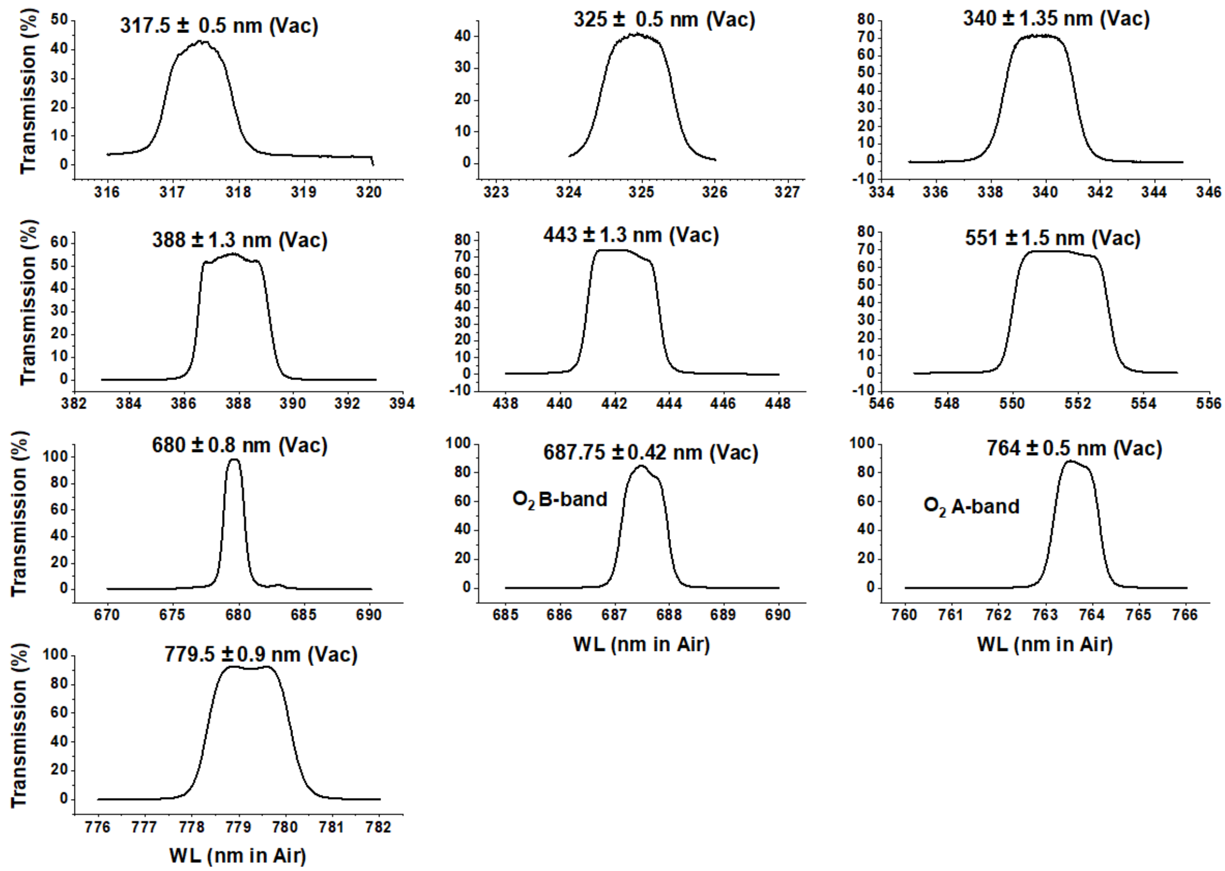
317.5 ± 0.5 nm (Vac)
325 ± 0.5 nm (Vac)
340 ± 1.35 nm (Vac)
388 ± 1.3 nm (Vac)
443 ± 1.3 nm (Vac)
551 ± 1.5 nm (Vac)
680 ± 0.8 nm (Vac)
687.75 ± 0.42 nm (Vac)
O_2 B-band
764 ± 0.5 nm (Vac)
O_2 A-band
779.5 ± 0.9 nm (Vac)
Transmission (%)
WL (nm in Air)

f01

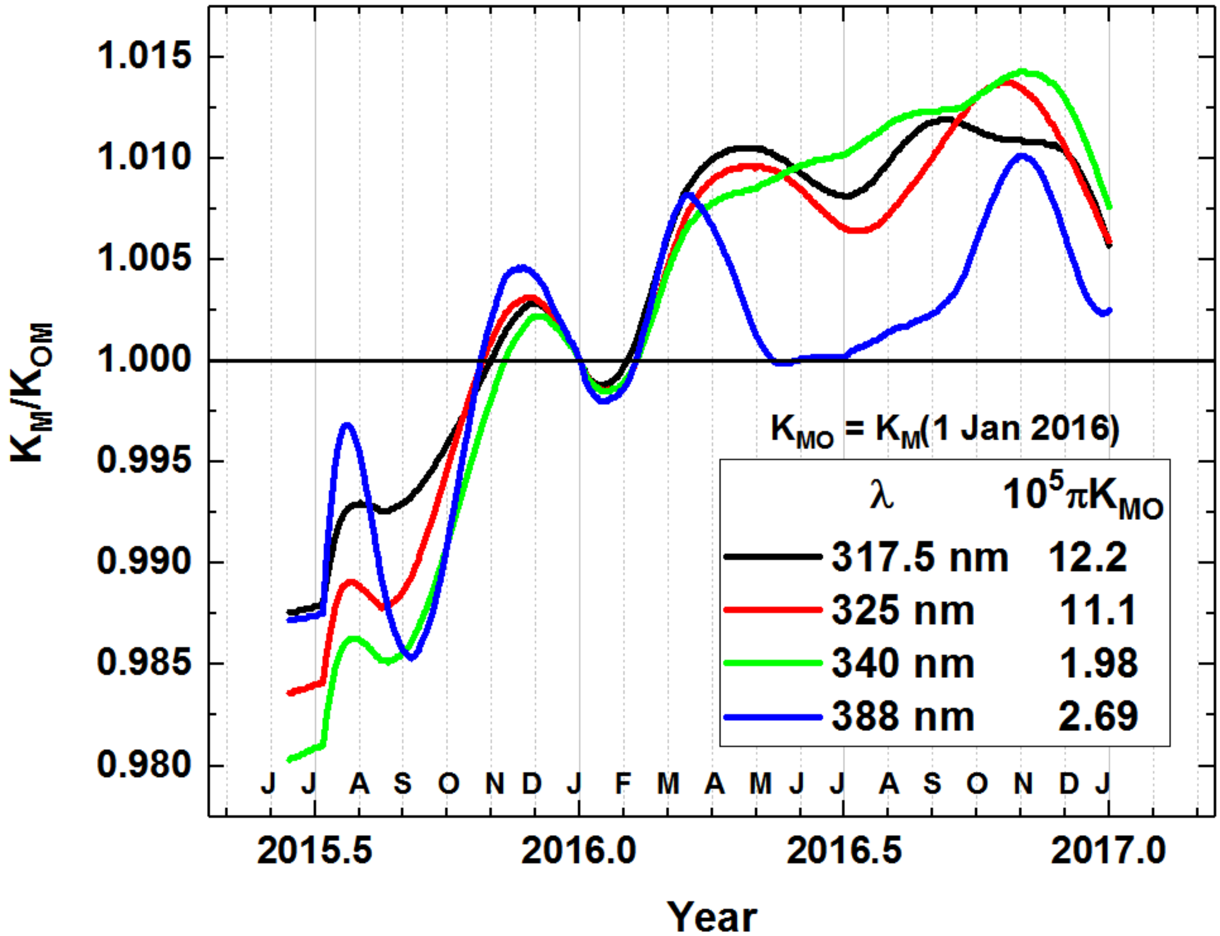
1.015
1.010
1.005
1.000
0.995
0.990
0.985
0.980
K_M/K_OM
J J A S O N D J F M A M J J A S O N D J
2015.5
2016.0
2016.5
2017.0
Year
K_MO = K_M(1 Jan 2016)
λ
10^5πK_MO
317.5 nm 12.2
325 nm 11.1
340 nm 1.98
388 nm 2.69

f02

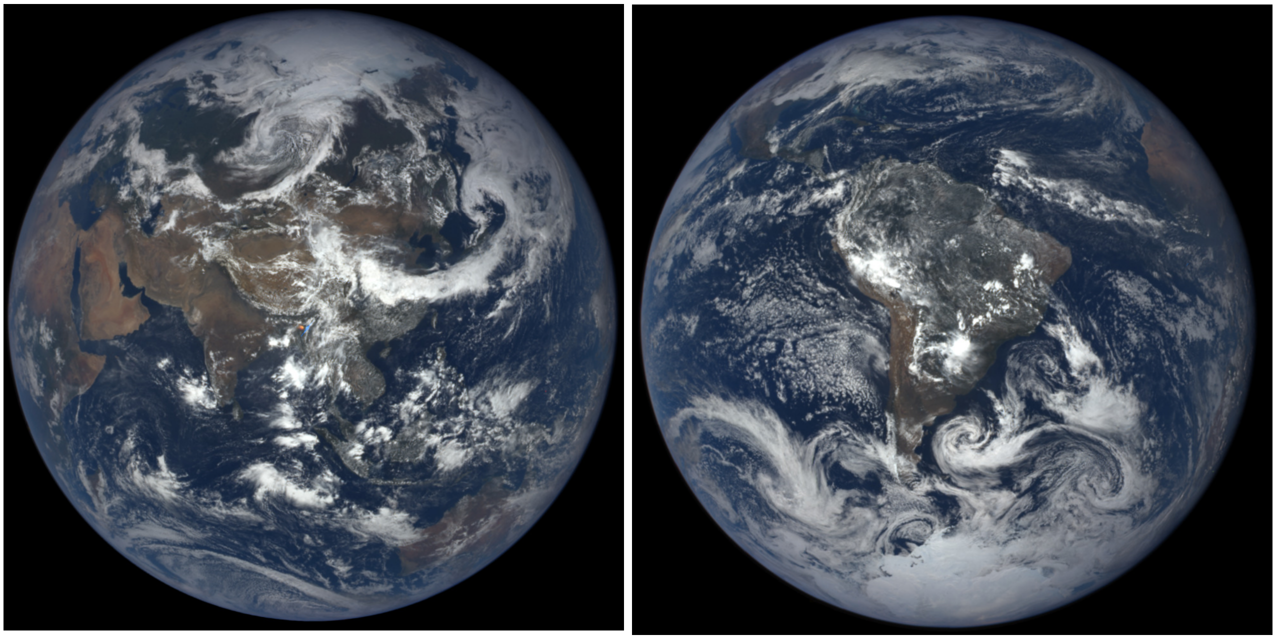

f03

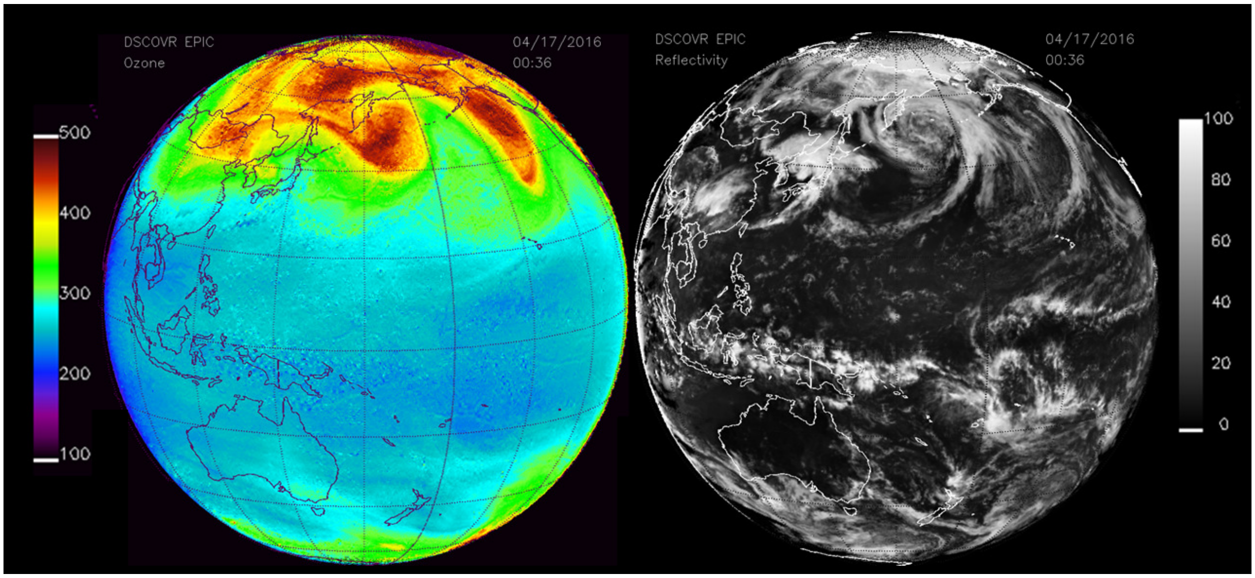
DSCOVR EPIC
Ozone
04/17/2016
00:36
500
400
300
200
100
DSCOVR EPIC
Reflectivity
04/17/2016
00:36
100
80
60
40
20
0

f04

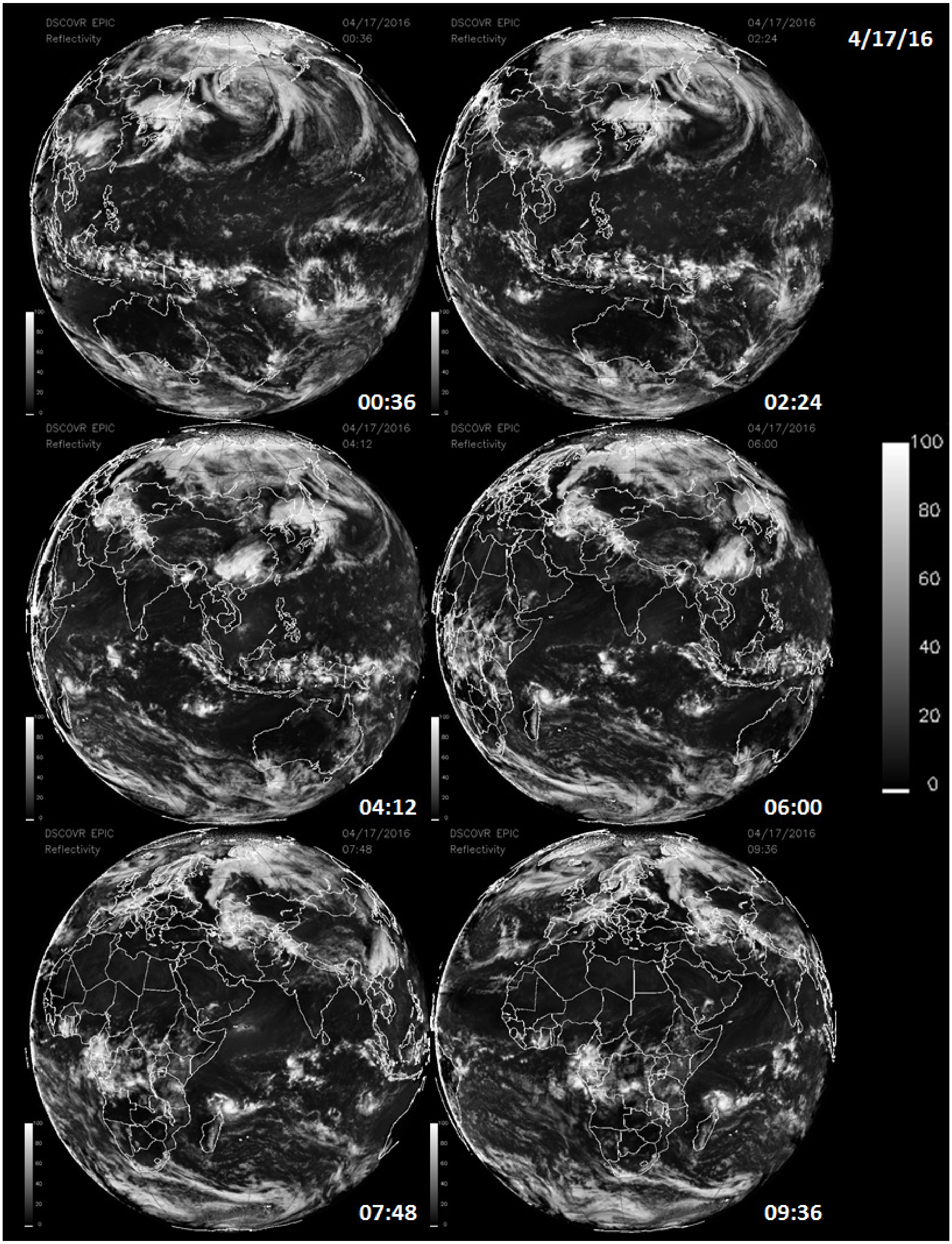

DSCOVR EPIC
Reflectivity
04/17/2016
00:36
02:24
04:12
06:00
07:48
09:36
4/17/16
100
80
60
40
20
0

f05

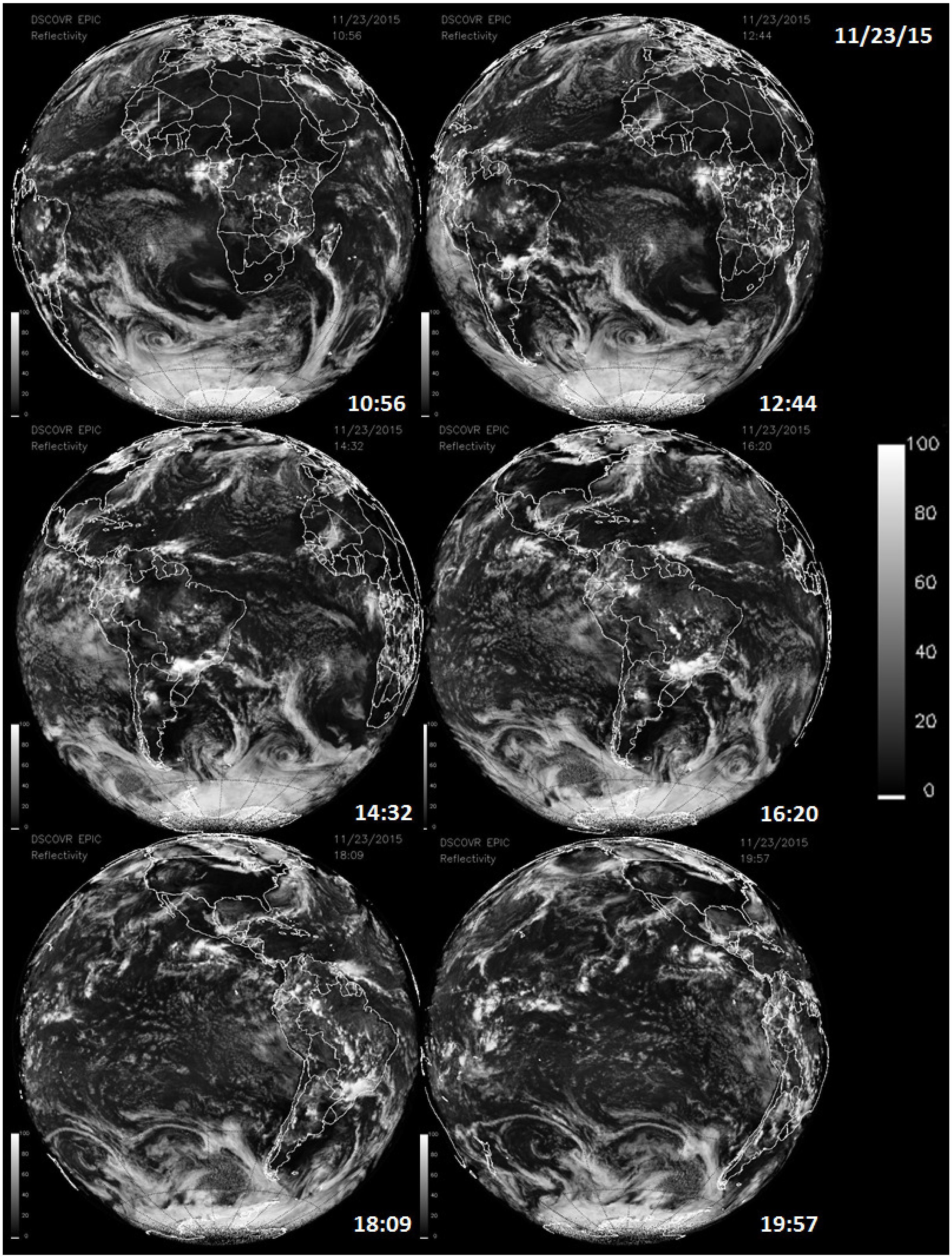
DSCOVR EPIC
Reflectivity
11/23/2015
10:56
DSCOVR EPIC
Reflectivity
11/23/2015
12:44
11/23/15
10:56
12:44
DSCOVR EPIC
Reflectivity
11/23/2015
14:32
DSCOVR EPIC
Reflectivity
11/23/2015
16:20
100
80
60
40
20
0
14:32
16:20
DSCOVR EPIC
Reflectivity
11/23/2015
18:09
DSCOVR EPIC
Reflectivity
11/23/2015
19:57
18:09
19:57

f06

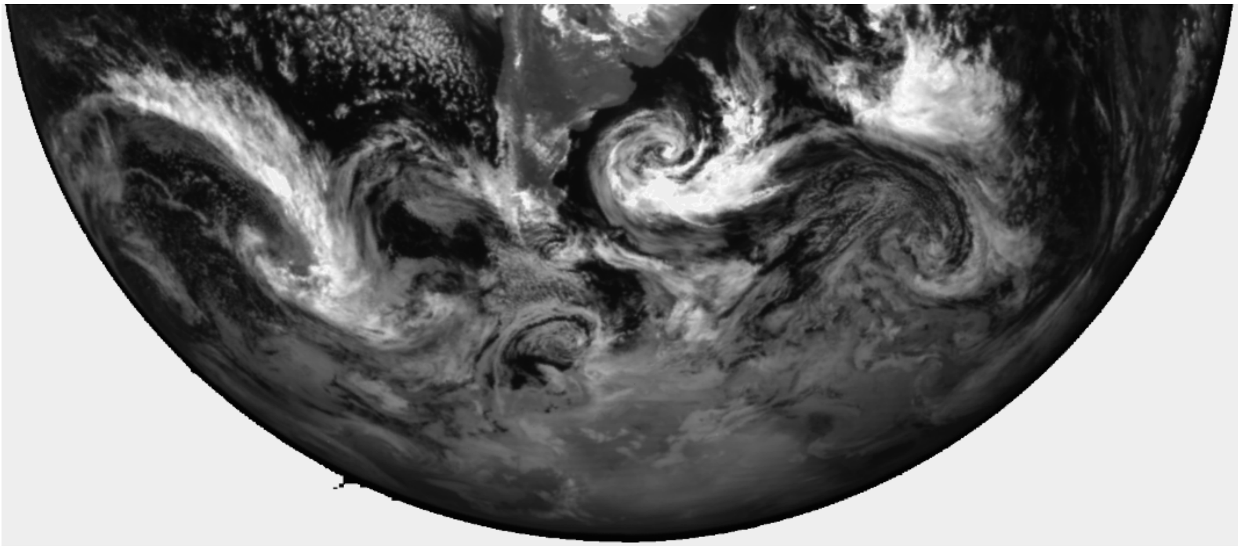

f07

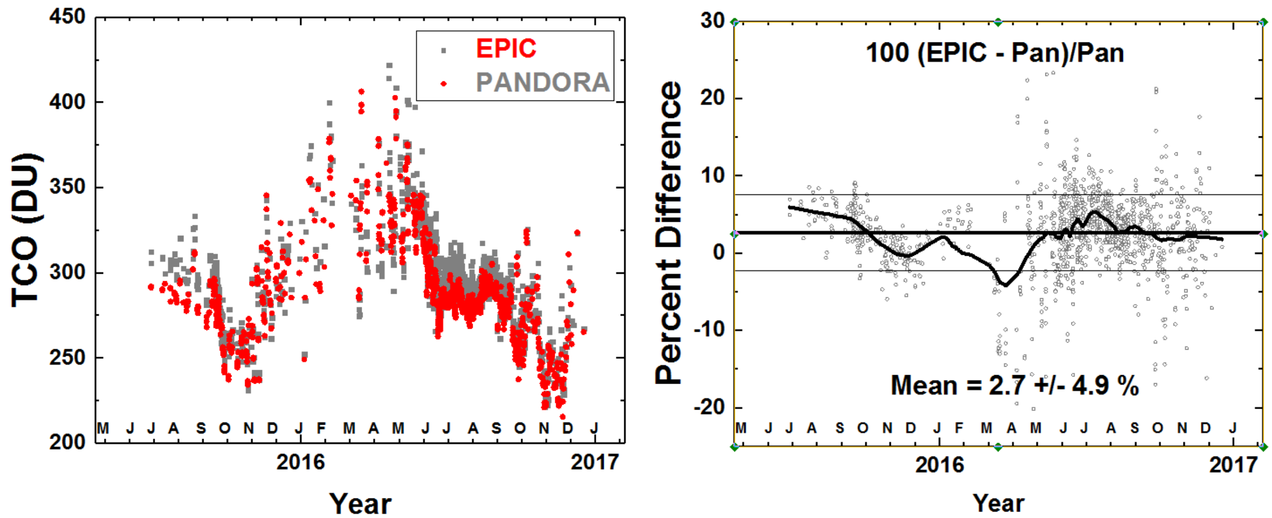
EPIC
PANDORA
TCO (DU)
450
400
350
300
250
200
M J J A S O N D J F M A M J J A S O N D J
2016
2017
Year
100 (EPIC - Pan)/Pan
Percent Difference
30
20
10
0
-10
-20
Mean = 2.7 +/- 4.9 %

f08

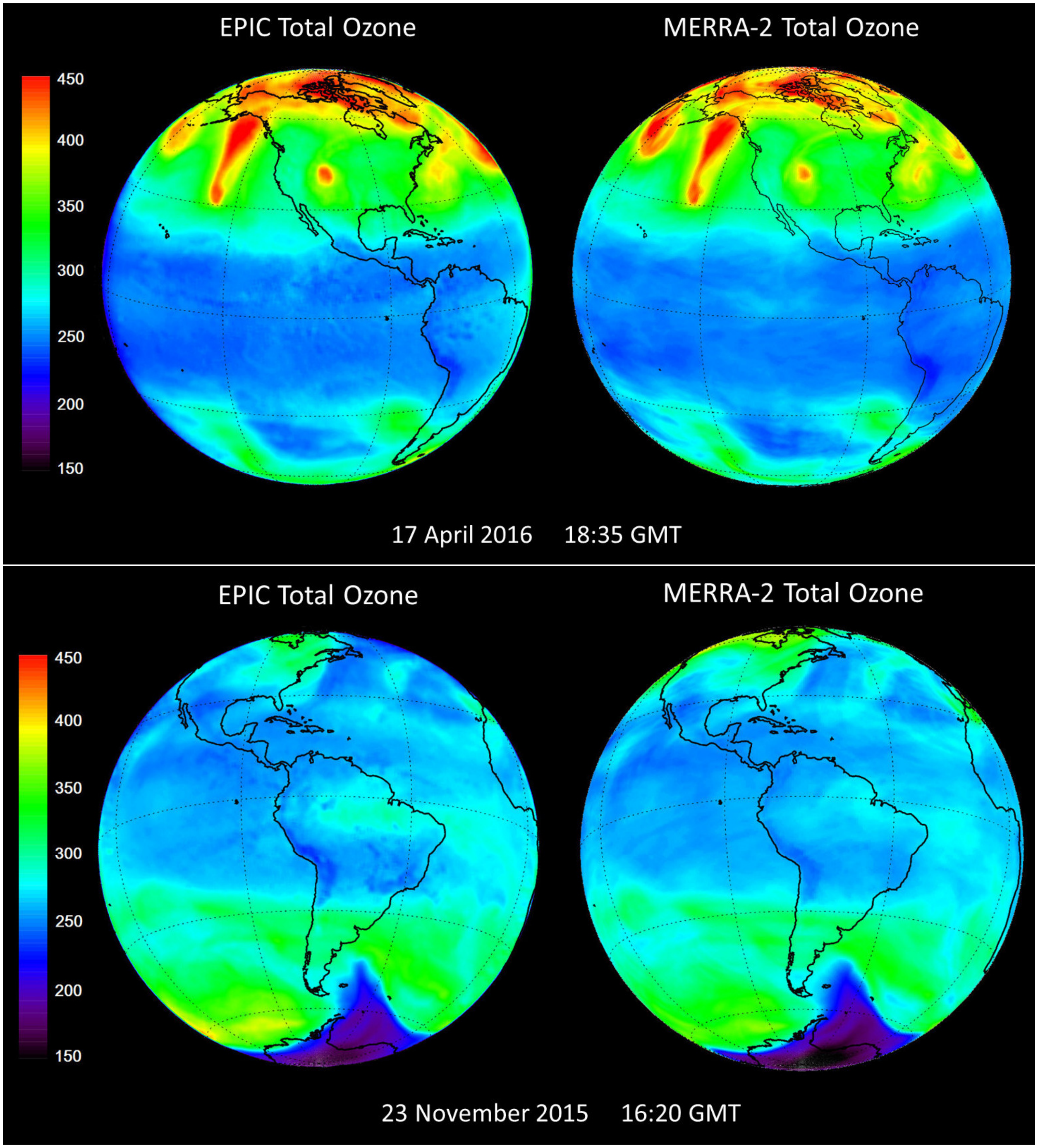
EPIC Total Ozone
MERRA-2 Total Ozone
450
400
350
300
250
200
150
17 April 2016 18:35 GMT
EPIC Total Ozone
MERRA-2 Total Ozone
450
400
350
300
250
200
150
23 November 2015 16:20 GMT

f09

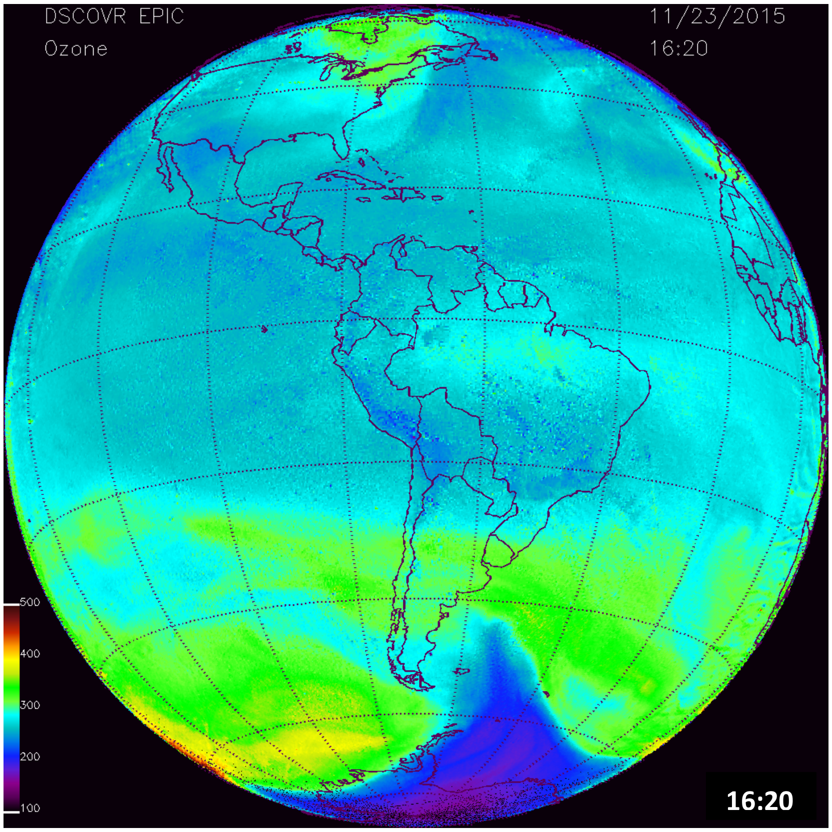

f10

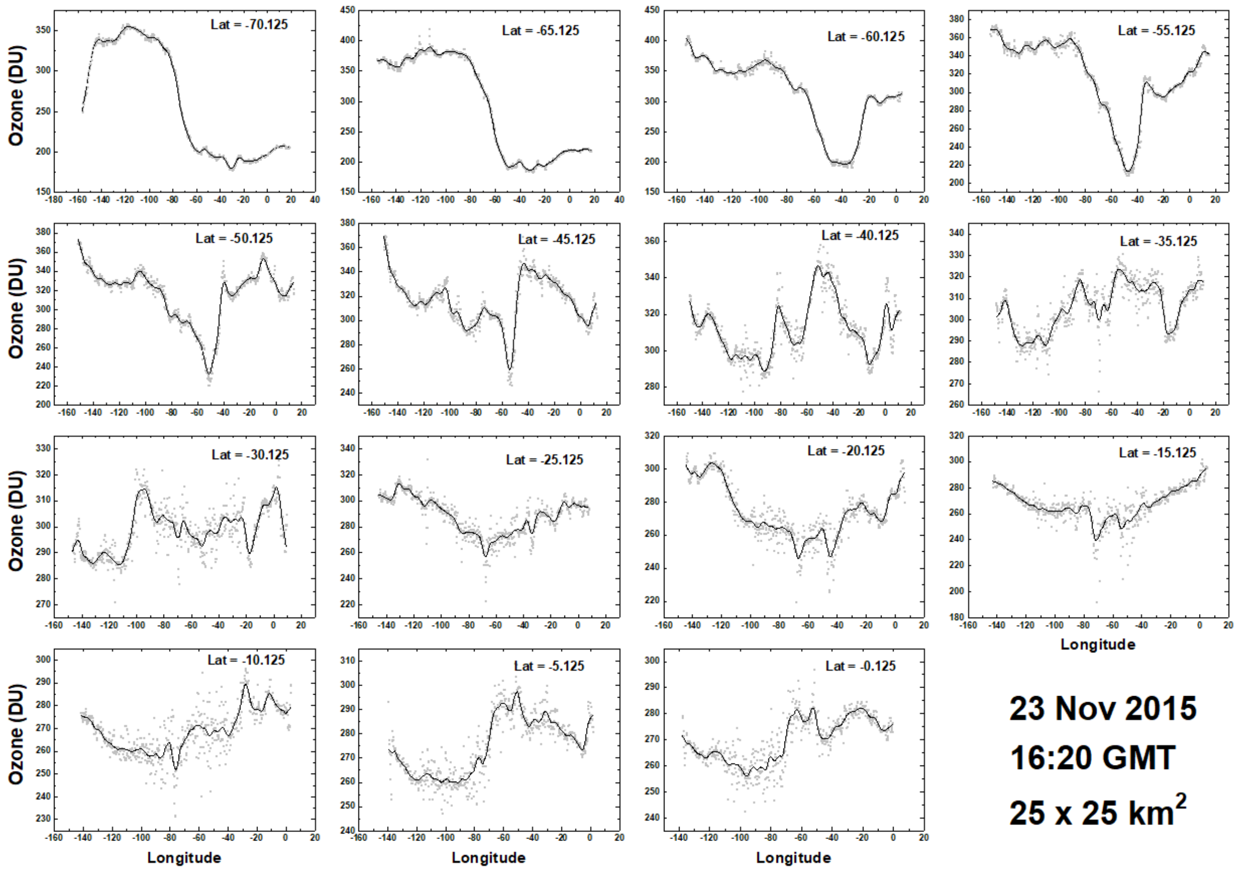
Lat = -70.125
Lat = -65.125
Lat = -60.125
Lat = -55.125
Lat = -50.125
Lat = -45.125
Lat = -40.125
Lat = -35.125
Lat = -30.125
Lat = -25.125
Lat = -20.125
Lat = -15.125
Lat = -10.125
Lat = -5.125
Lat = -0.125
Ozone (DU)
Longitude
23 Nov 2015
16:20 GMT
25 x 25 km^2

f11

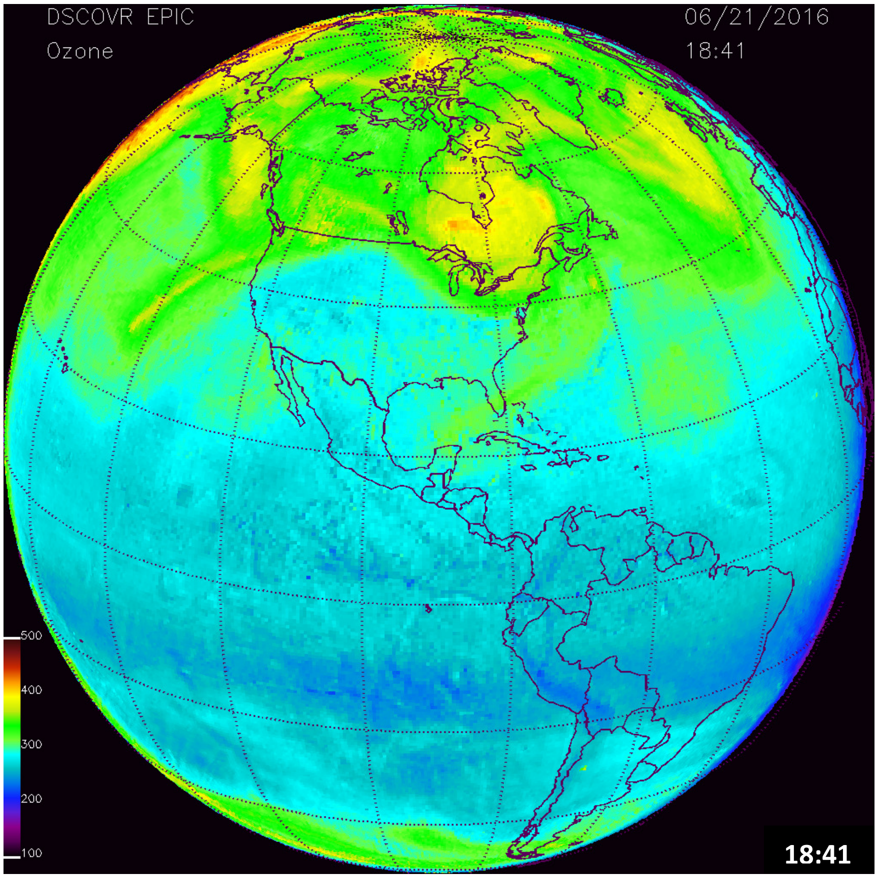

f12

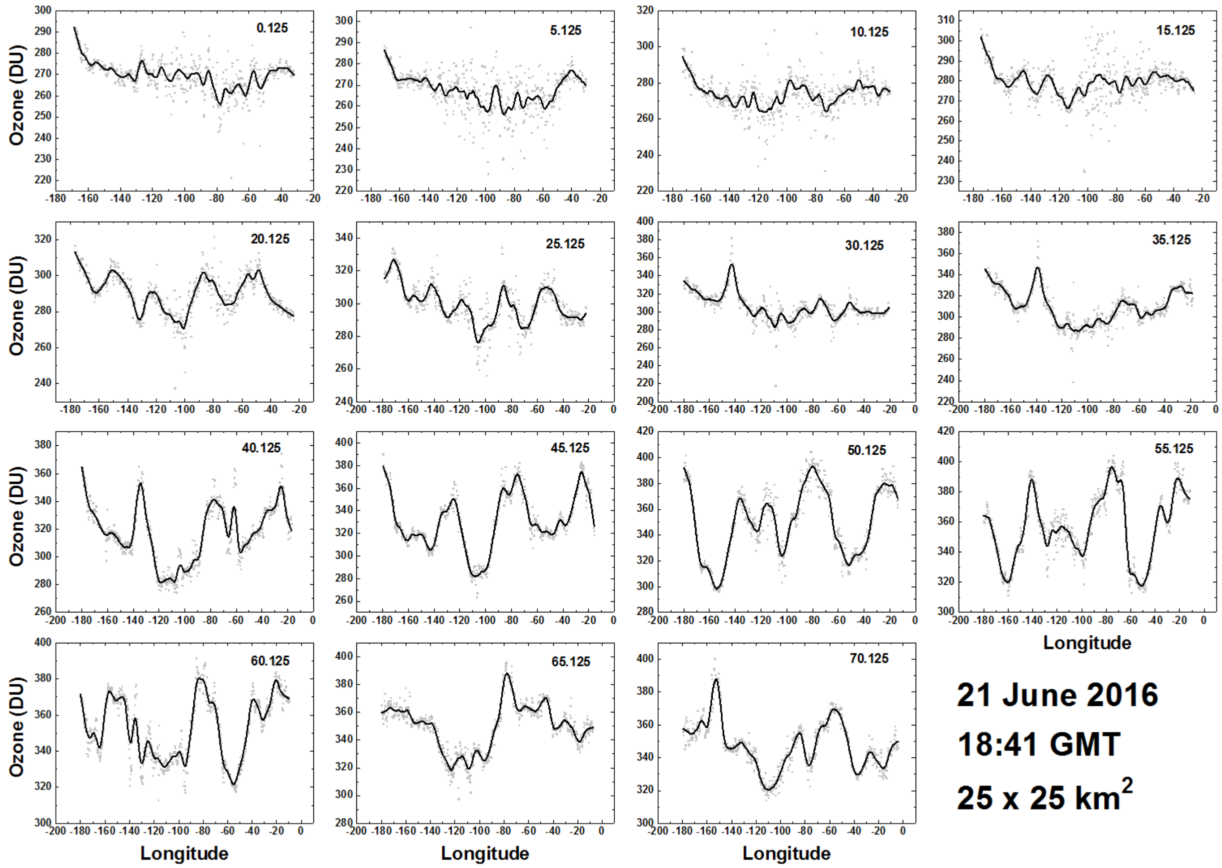
0.125
5.125
10.125
15.125
20.125
25.125
30.125
35.125
40.125
45.125
50.125
55.125
60.125
65.125
70.125
Ozone (DU)
Longitude
21 June 2016
18:41 GMT
25 x 25 km²

f13

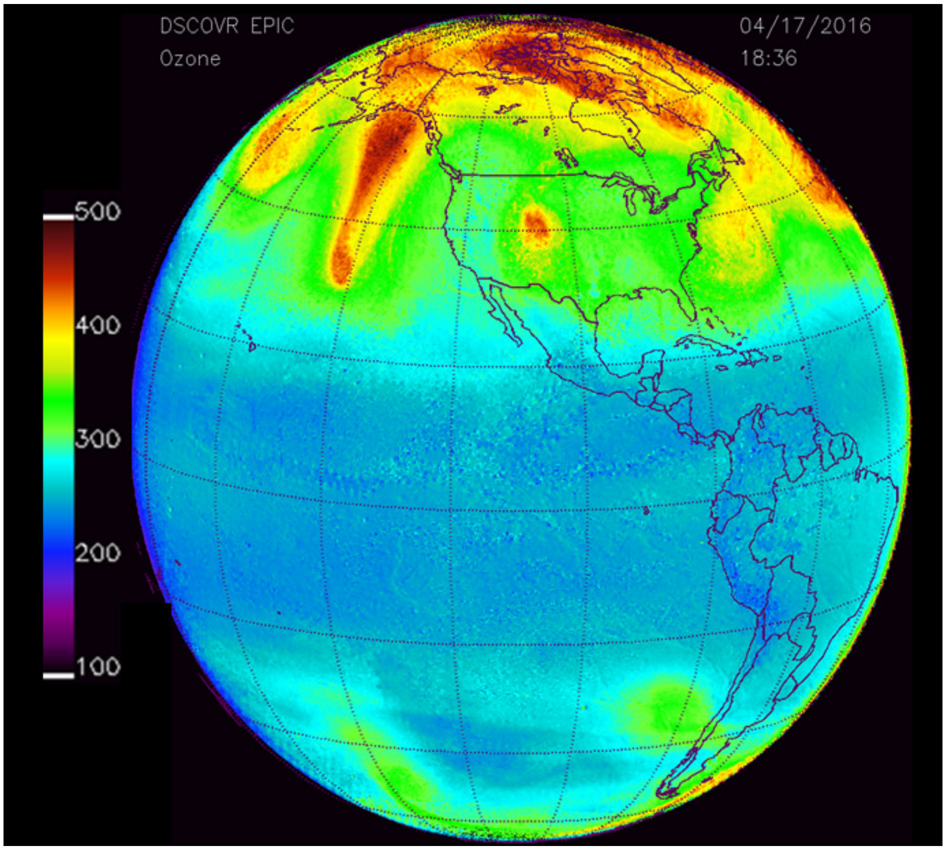

f14

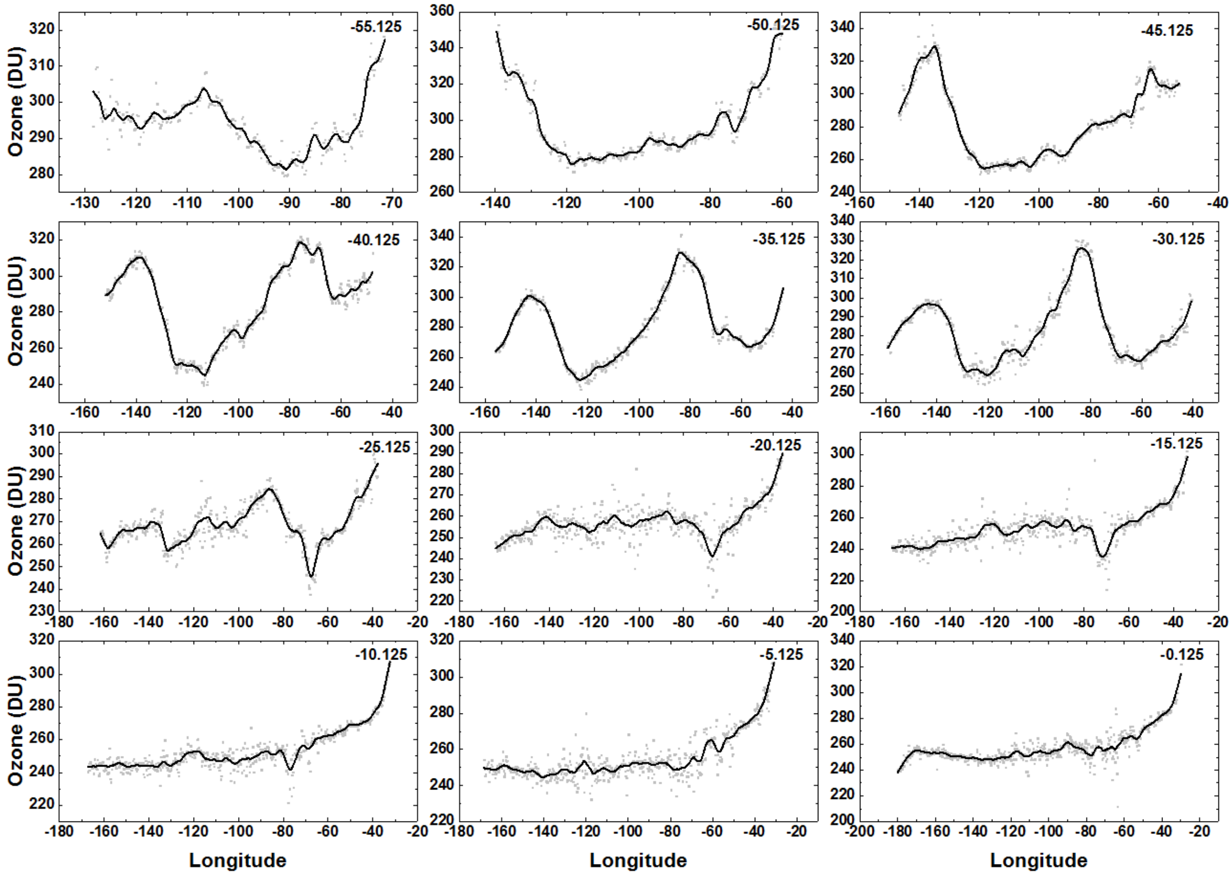
-55.125
-50.125
-45.125
-40.125
-35.125
-30.125
-25.125
-20.125
-15.125
-10.125
-5.125
-0.125
Ozone (DU)
Longitude

f15

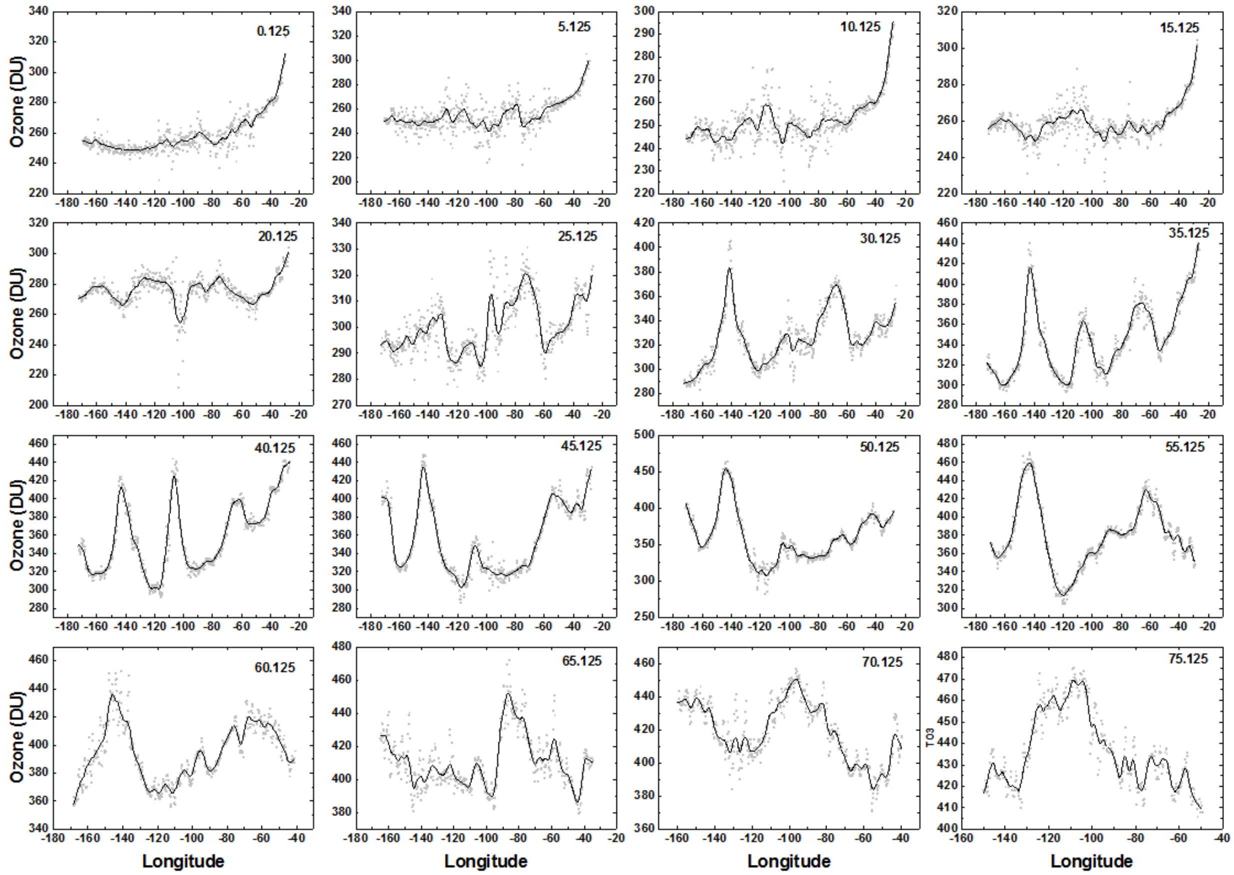
0.125
5.125
10.125
15.125
20.125
25.125
30.125
35.125
40.125
45.125
50.125
55.125
60.125
65.125
70.125
75.125
Ozone (DU)
TO3
Longitude

f16

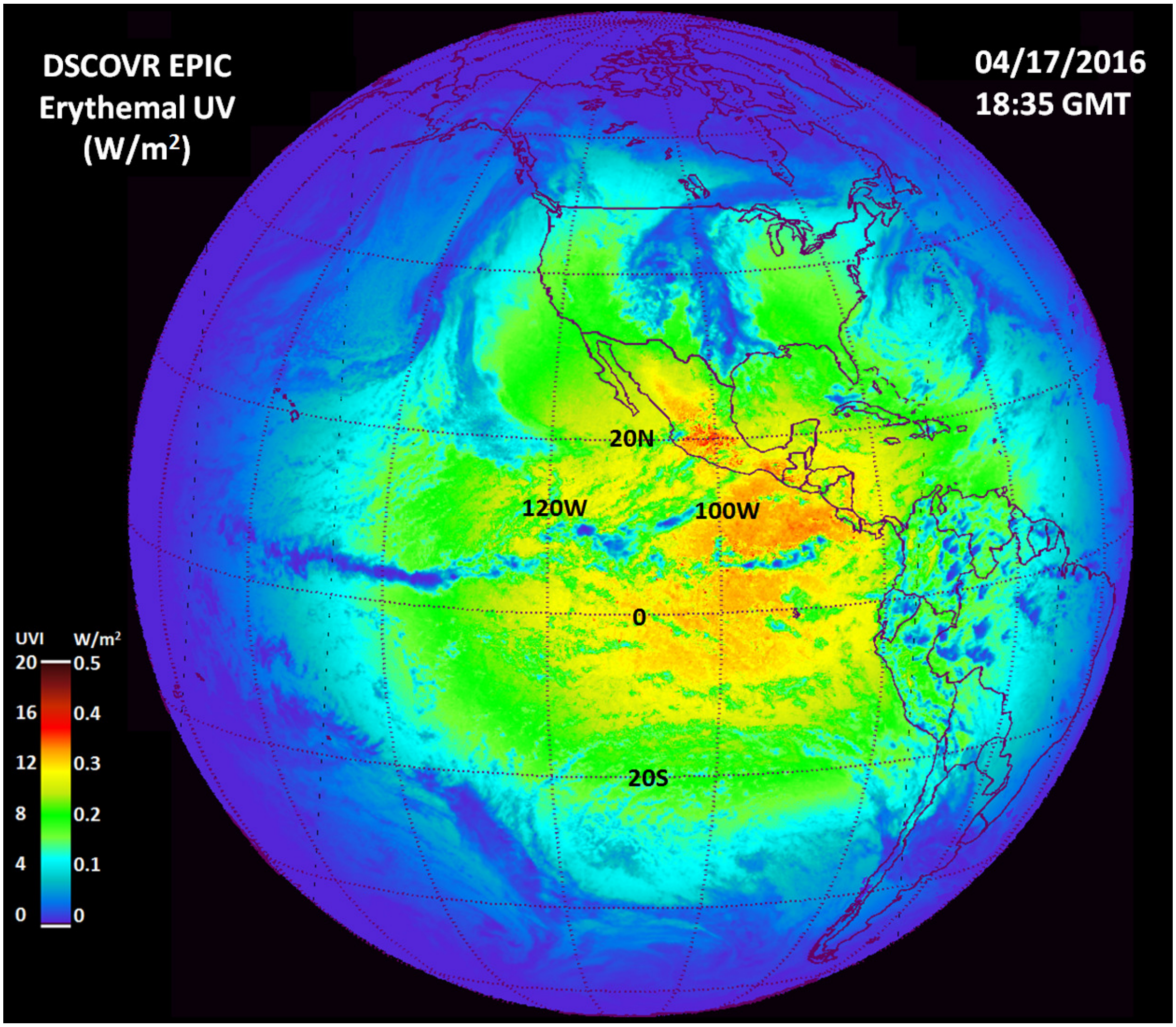
DSCOVR EPIC
Erythemal UV
(W/m²)
04/17/2016
18:35 GMT
20N
120W
100W
0
20S
UVI
W/m²
20
16
12
8
4
0
0.5
0.4
0.3
0.2
0.1
0

f17

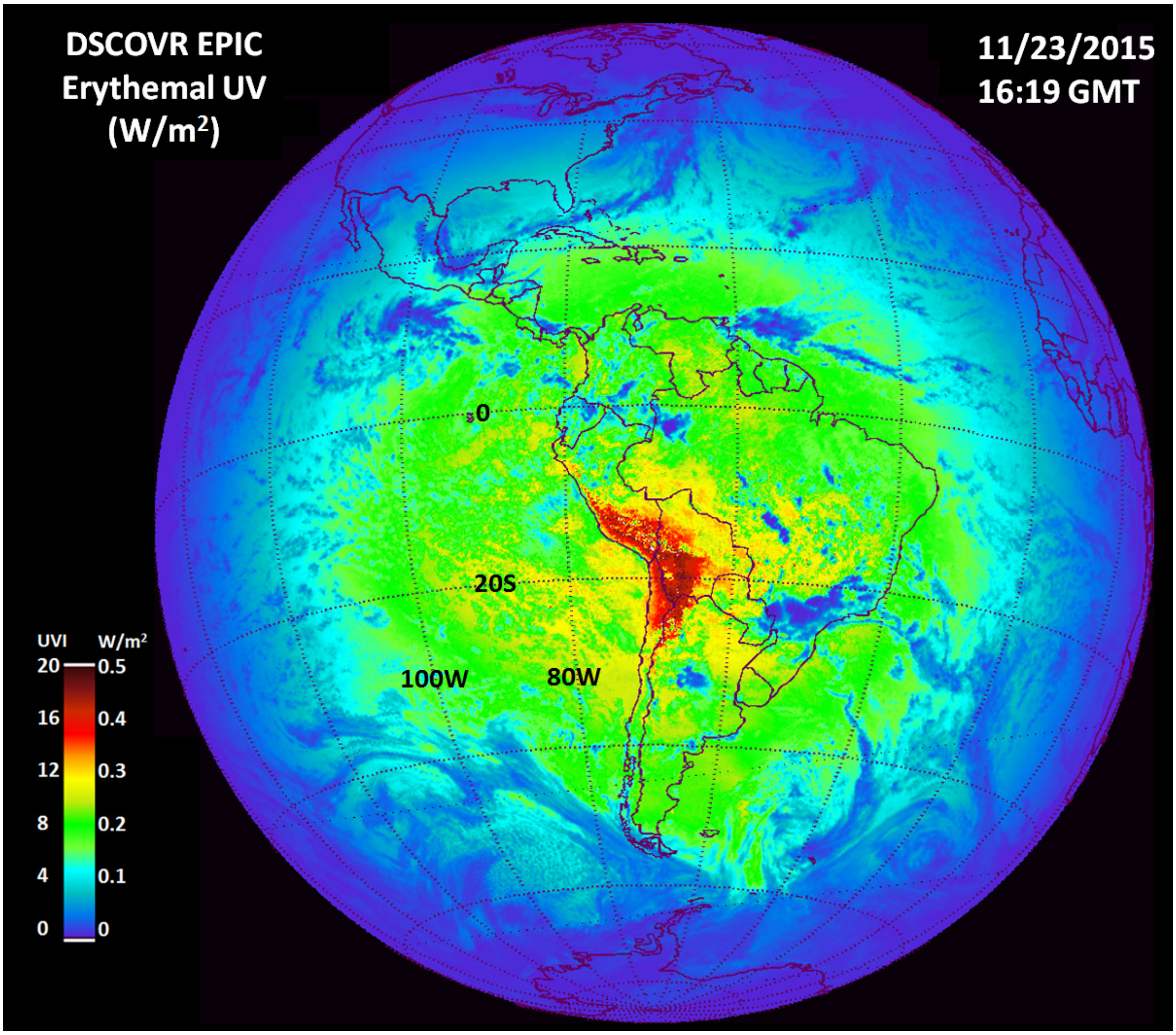
DSCOVR EPIC
Erythemal UV
(W/m2)
11/23/2015
16:19 GMT
0
20S
100W
80W
UVI
W/m2
20
16
12
8
4
0
0.5
0.4
0.3
0.2
0.1
0

f18

764

765

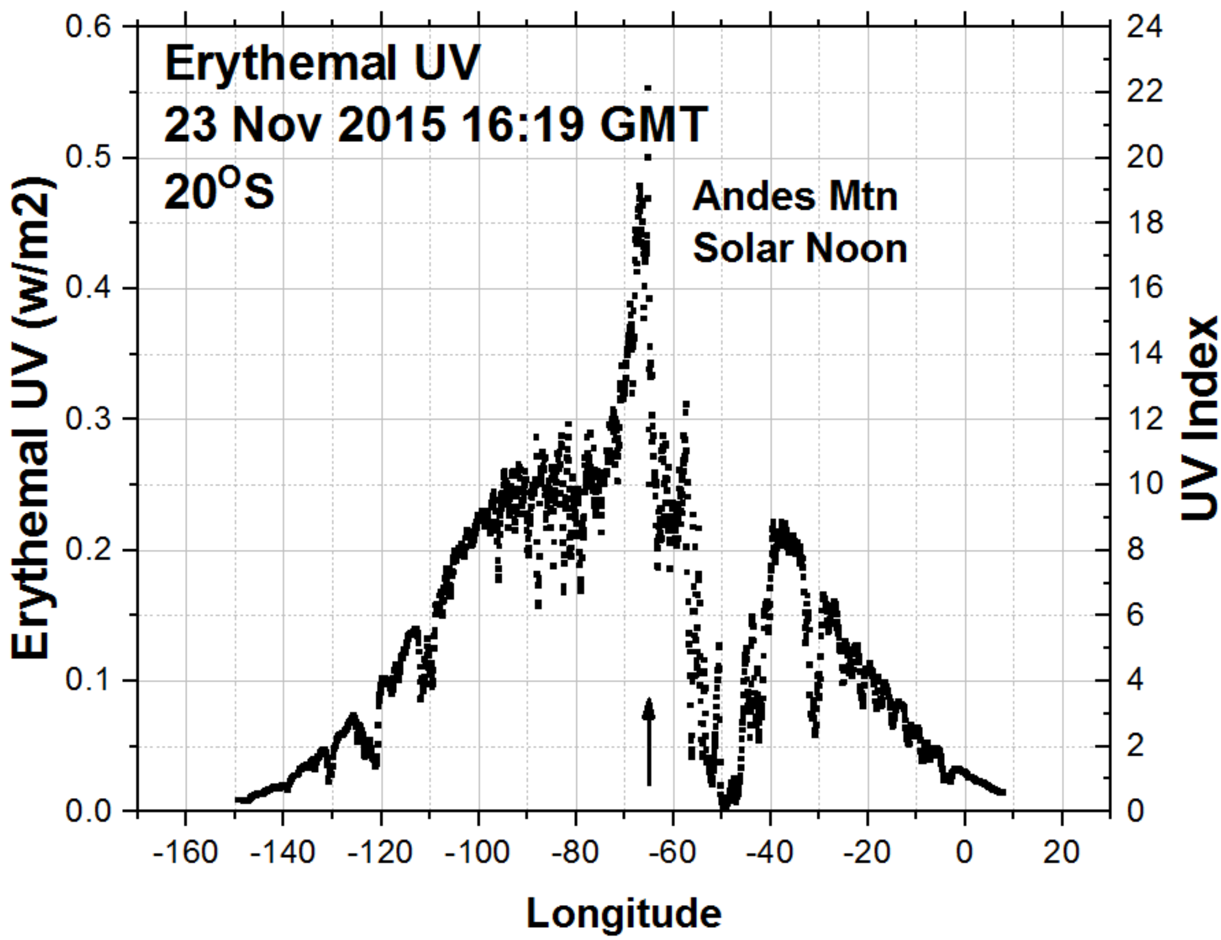
Erythemal UV
23 Nov 2015 16:19 GMT
20OS
Andes Mtn
Solar Noon
Erythemal UV (w/m2)
UV Index
Longitude
0.0
0.1
0.2
0.3
0.4
0.5
0.6
0
2
4
6
8
10
12
14
16
18
20
22
24
-160
-140
-120
-100
-80
-60
-40
-20
0
20

f19

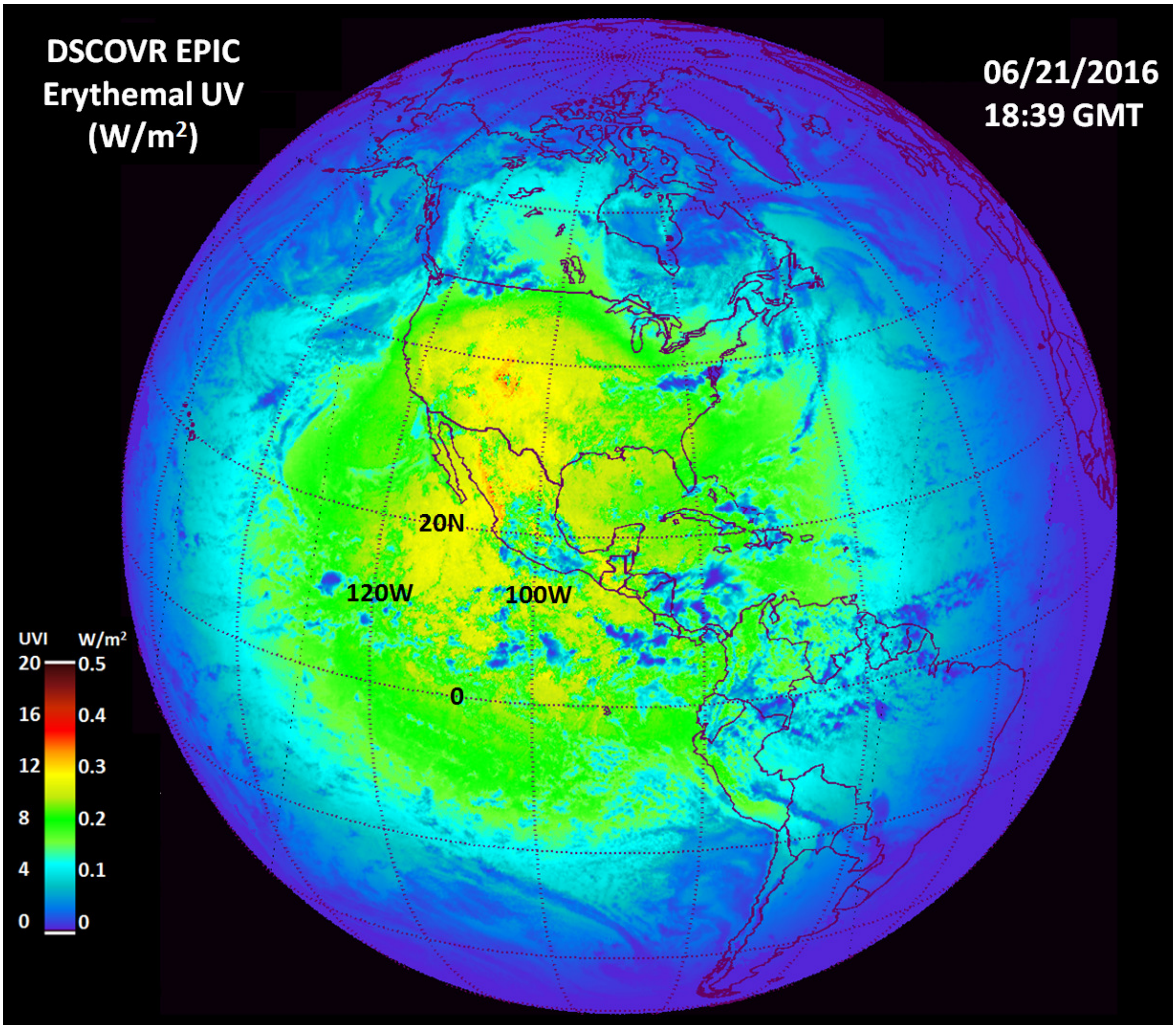
DSCOVR EPIC
Erythemal UV
(W/m²)
06/21/2016
18:39 GMT
20N
120W
100W
0
UVI
W/m²
20
0.5
16
0.4
12
0.3
8
0.2
4
0.1
0
0

f20

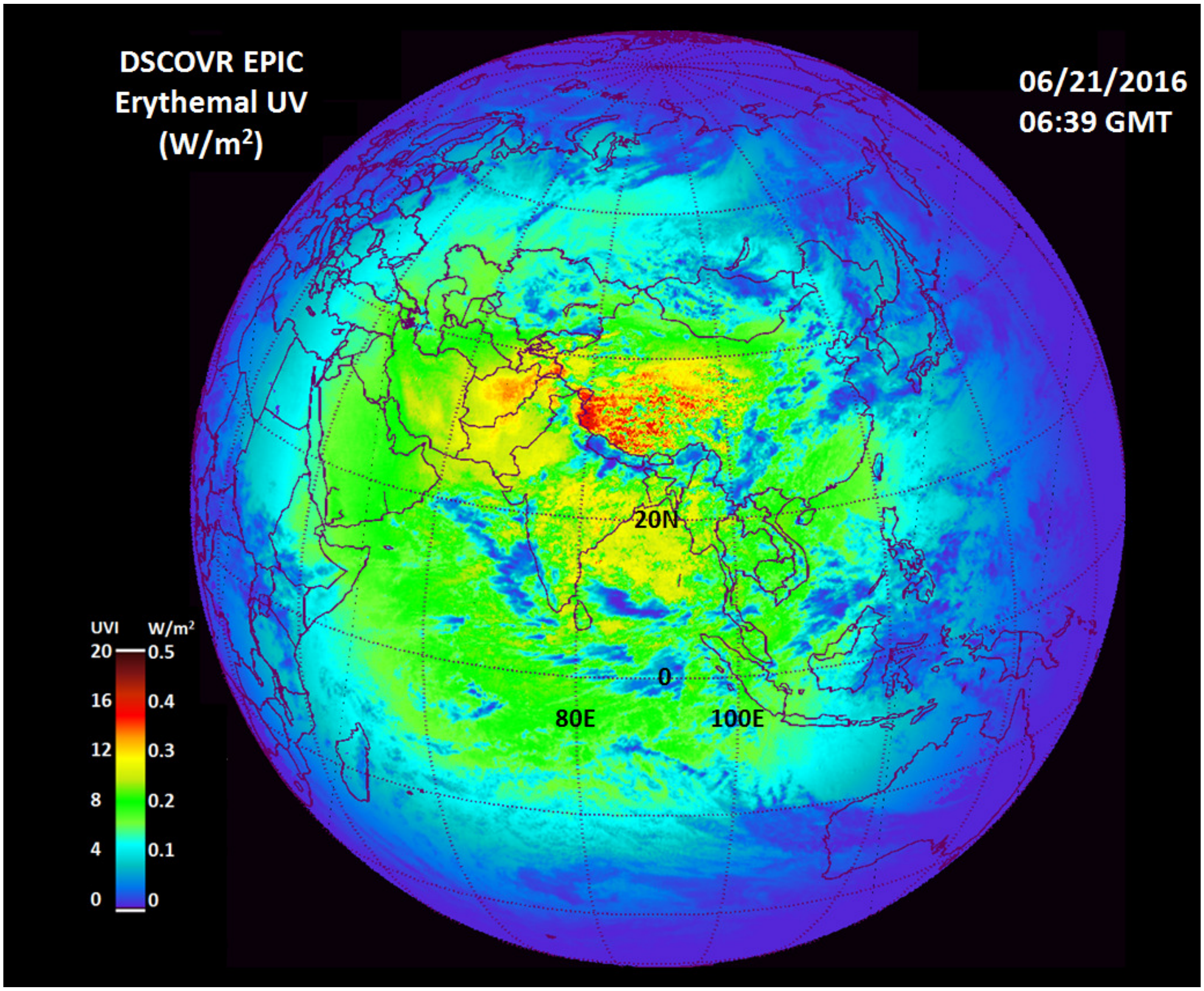
DSCOVR EPIC
Erythemal UV
(W/m²)
06/21/2016
06:39 GMT
UVI
W/m²
20
0.5
16
0.4
12
0.3
8
0.2
4
0.1
0
0
20N
0
80E
100E

f21

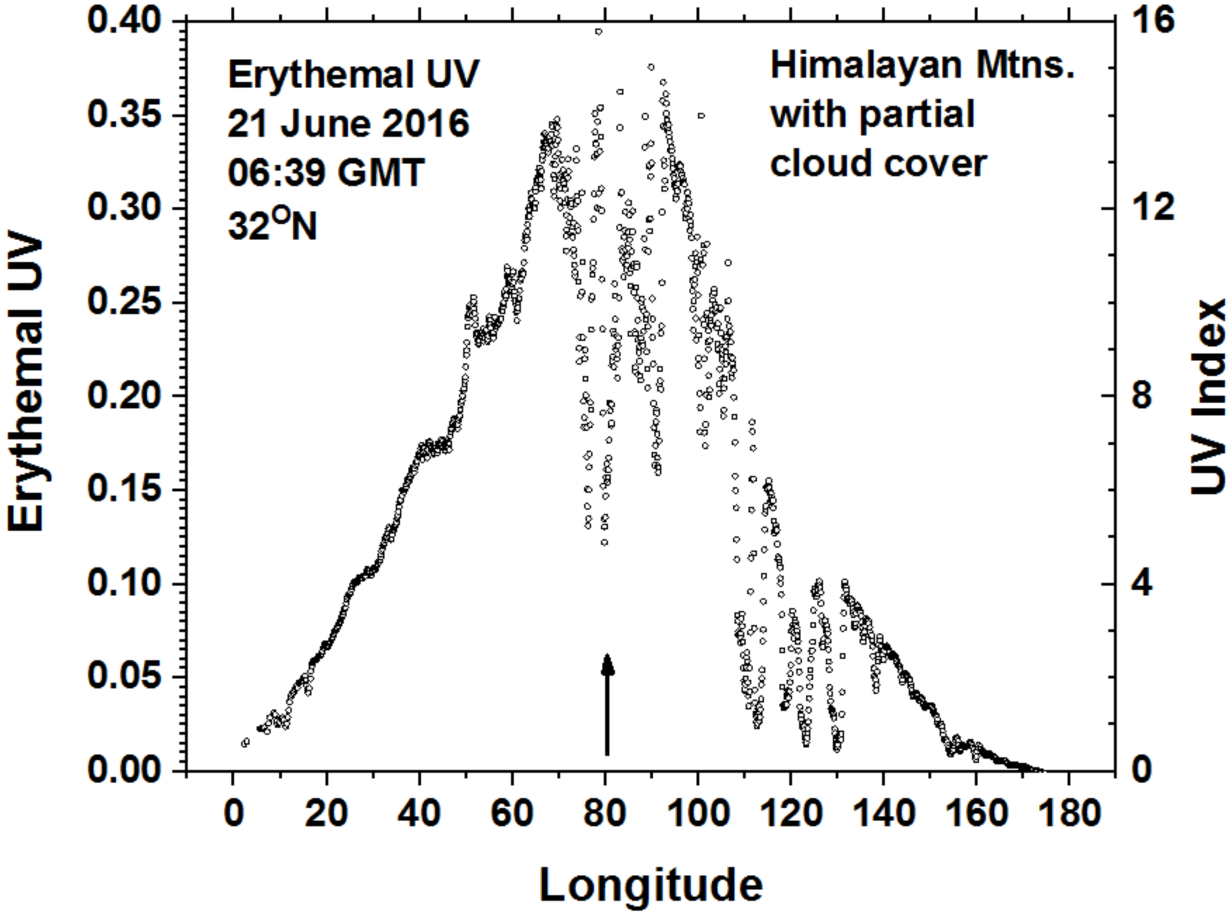
Erythemal UV
21 June 2016
06:39 GMT
32^{O}N
Himalayan Mtns.
with partial
cloud cover
Erythemal UV
UV Index
Longitude
0.40
0.35
0.30
0.25
0.20
0.15
0.10
0.05
0.00
0
20
40
60
80
100
120
140
160
180
16
12
8
4
0

f22

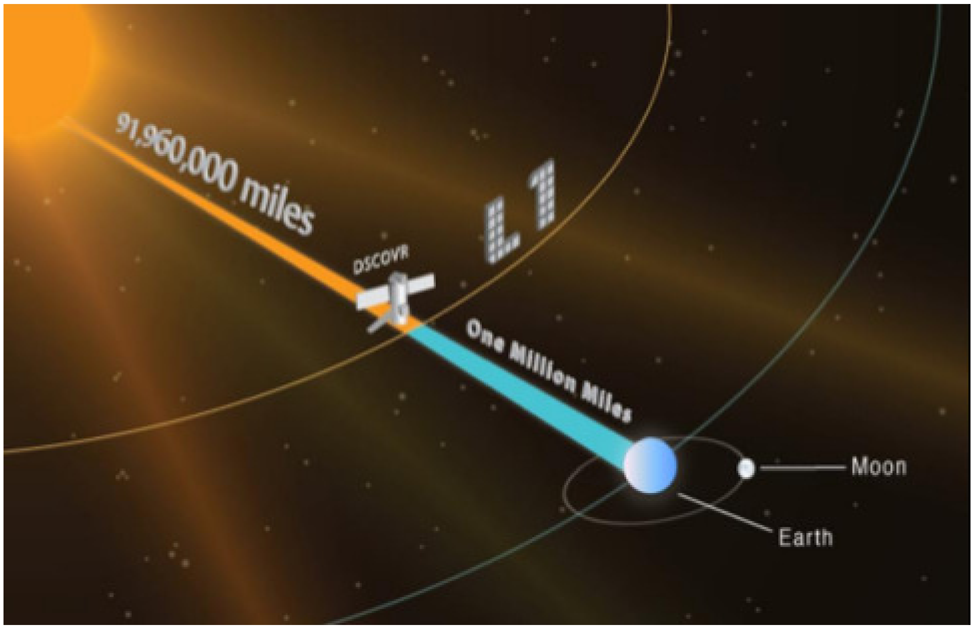

fA1

778